THESIS FOR THE DEGREE OF DOCTOR OF PHILOSOPHY

Synthesis of tailored nanoparticles for palladium-based oxidation catalysts

Yanyue Feng

Department of Chemistry and Chemical Engineering
CHALMERS UNIVERSITY OF TECHNOLOGY

Göteborg, Sweden 2023

Synthesis of tailored nanoparticles for palladium-based oxidation catalysts
YANYUE FENG
ISBN 978-91-7905-800-5

Doktorsavhandlingar vid Chalmers tekniska högskola
Ny serie Nr. 5266
ISSN 0346-718X

Department of Chemistry and Chemical Engineering
Chalmers University of Technology
SE-412 96 Göteborg
Sweden
Telephone +46 31 772 1000

Cover:
CO oxidation over Al_2O_3 supported Au@Pd core@shell nanoparticles.

Printed by Chalmers Digitaltryck
Göteborg, Sweden 2023

Synthesis of tailored nanoparticles for palladium-based oxidation catalysts
YANYUE FENG
Department of Chemistry and Chemical Engineering
Chalmers University of Technology

Abstract

The immense changes of physical and chemical properties of materials caused by the transition from microscale to nanoscale have been attracting scientific attention for decades. Rapid development of modern techniques triggers the attention on the multicomponent nanoparticle catalysts with enhanced catalytic activities. In this thesis, the Au@Pd core@shell nanoparticle system and highly dispersed Pd/CeO_2 and Pt/CeO_2 are investigated in order to achieve highly active oxidation catalysts.

The Au@Pd core@shell nanoparticles were synthesized by a two-step seeded growth method. The effects of temperature and Pd/Au molar ratio on the morphology of Au@Pd core@shell nanoparticles were studied. The effect of the Au core on the Pd surface properties was studied by systematically varying the core/shell ratio. Highly dispersed Pd/CeO_2 and Pt/CeO_2 were prepared by incipient wetness impregnation. High-resolution transmission electron microscopy (HRTEM), high-angle annular dark field scanning transmission electron microscopy (HAADF-STEM), and energy-dispersive X-ray spectroscopy (EDS) line scanning were utilized to investigate the morphology of the nanoparticle catalysts. Chemical composition was measured by X-ray fluorescence (XRF), and the surface electron structure and chemical state were investigated by X-ray photoelectron spectroscopy (XPS). An environmental reaction cell was used to test the catalytic activity for the CO oxidation reaction. *In situ* diffuse reflectance infrared Fourier transform spectroscopy (DRIFTS) was used to study the surface species during CO adsorption and CO oxidation reaction conditions.

It is shown that Au@Pd core@shell nanoparticles with different Au core sizes and Pd shell thickness can be successfully synthesized and loaded onto alumina using precise synthesis conditions. Moreover, neither agglomeration nor destruction of the core@shell motif under CO oxidation reaction conditions could be observed, indicating good structural stability. Further, *in situ* infrared spectroscopy reveals that palladium surface properties in core@shell system differ to palladium only particles, suggesting electronic and structural modification of the Pd shell surface by the Au core. The Pd shell thickness must exceed 0.5 nm as to be active for CO oxidation at low temperatures.

Keywords: supported catalysts, Pd and Au@Pd core@shell nanoparticles, morphology and surface properties, *in situ* spectroscopy, CO oxidation

List of Publications

This thesis is based on the following appended papers

Paper I:
Synthesis and Characterization of Catalytically Active Au Core-Pd Shell Nanoparticles Supported on Alumina
Yanyue Feng, Andreas Schaefer, Anders Hellman, Mengqiao Di, Hanna Härelind, Matthias Bauer and Per-Anders Carlsson
Langmuir 2022, 38, 12859-12870

Paper II:
Effect of Au core size and Pd shell thickness on CO oxidation studied by systematic variation of the Au@Pd/Al_2O_3 model catalyst motif
Yanyue Feng, Anders Hellman, Andreas Schaefer, Mengqiao Di, Felix Hemmingsson, Hanna Härelind, Matthias Bauer and Per-Anders Carlsson
Manuscript

Paper III:
CO oxidation over highly dispersed palladium ceria catalysts
Yanyue Feng, Andreas Schaefer, Mengqiao Di, Hanna Härelind and Per-Anders Carlsson
Manuscript

Paper IV:
Chasing PtO_x species in ceria supported platinum during CO oxidation extinction with correlative *operando* spectroscopic techniques
Mengqiao Di, Kerry Simmance, Andreas Schaefer, Yanyue Feng, Felix Hemmingsson, Magnus Skoglundh, Tamsin Bell, David Thompsett, Lucy Idowu Ajakaiye Jensen, Sara Blomberg and Per-Anders Carlsson
Journal of Catalysis 409 (2022) 1-11

My Contribution

Paper I:
Responsible for all synthesis, experimental characterization (except XPS) and activity tests of the core-shell nanoparticles catalyst. Wrote the first draft of the manuscript and responsible for the submission.

Paper II:
Responsible for all synthesis, experimental characterization (except XPS) and activity test of the core-shell nanoparticles catalyst. Wrote the first draft of the manuscript.

Paper III:
Responsible for all experimental characterization and evaluation of the Pd/CeO_2 catalyst. Wrote the first manuscript draft.

Paper IV:
Responsible for TEM imaging and EDS mapping. Co-authored the manuscript.

List of Figures

Notation

DRIFTS Diffuse reflectance infrared fourier transform spectroscopy.

EDS energy-dispersive X-ray spectroscopy.

HAADF-STEM high angle annular dark field scanning transmission electron microscopy.

HRTEM high resolution transmission electron microscopy.

IR Infrared spectroscopy.

MSI metal support interaction.

PXRD Powder X-ray diffraction.

TEM transmission electron microscopy.

XPS X-ray photoelectron spectroscopy.

XRF X-ray fluorescence.

Contents

1 Introduction

Catalysis is regarded as a facilitating technology providing possibilities for the utilization of raw materials through functionalization, which finds applications in many fields [1]. For instance, it plays an important role in fuel and chemical industries with almost 90% of the chemical processes involving catalysts in some of their steps [2]. A survey from U.S. industries shows that more than 60% of essential 63 products and 90% of 34 important process innovations between 1930 to 1980 have been made commercially viable thanks to catalysts. Catalysis at an interface is defined as heterogeneous catalysis, in which the reactants and the catalysts are in different phases [1]. Environmental studies of heterogeneous catalysis could be dated back to the early 1800s when Faraday first examined the ability of platinum to facilitate oxidation reactions. From then on, many other catalytic processes have been developed, such as hydrogenation, dehydrogenation, polymerization, etc. Those catalytic reactions played important roles in the industrial revolution [3]. Nowadays, with the arising of environmental and climate issues, catalysts play even more roles in the sustainable development of our society.

Among the different types of catalysts, transition metal nanoparticles, which are clusters comprising tens to thousands of metal atoms [1], are of great interest in both academic research and industrial applications due to their large surface-to-volume ratio, exposing many catalytic sites, and their good catalytic properties [4]. For example, Au-based catalysts show activity in low-temperature CO oxidation [5], acetylene hydro-chlorination [6], selective oxidation of alcohols [7], etc. Pd-based catalysts are also known for the production of fine chemicals, such as the sustainable and cleaner production of 2,5-dimethyl furan (DMF) as liquid biofuel [8], oxidation and electro-oxidation of alcohols into carboxylate [9, 10], direct oxidation of H_2 to H_2O_2 [11] etc. Pt-based catalysts are used in fuel cells for hydrogen evolution reaction [12].

For practical reasons, loading nanoparticles onto support materials (*e.g.* SiO_2, Al_2O_3, CeO_2 and TiO_2) is considered an effective way to handle and stabilize the nanoparticles. The supported noble metal nanoparticle catalyst plays a critical role in many industrial processes [13]. For instance, silica-supported Pd nanoparticle catalysts were observed to have high efficiency for Suzuki coupling, *i.e.* an organic cross-coupling reaction [14]. Supported Pt nanoparticle catalysts are known to have good catalytic activity for NO oxidation [15] and alcohol oxidation [16].

Thanks to the development of modern synthesis and characterization

techniques, catalysts can be tailored to achieve enhanced catalytic activity, selectivity and stability. There are several ways to accomplish this goal. For example, involving active supports to modify the catalysts, or forming bimetallic system (alloy or core@shell system). Regarding the active support, reducible metal oxides, such as CeO_2, are commonly used because of their dynamic oxygen storage ability [17], as well as the strong metal-support-interaction (MSI) [18]. For the bimetallic system, supported bimetallic nanoparticle catalysts with core-shell structures are of great interest due to the synergies between cores and shells, and used in many different fields, such as catalysis [19, 20], bio-nanotechnology [21], energy storage materials [22] and so on. There are three effects that co-exist in core-shell systems, which are ligand effects, ensemble effects and geometric effects [23]. Ligand effects involve the alternation of the d-band center of the shell material, which is caused by a charge transfer between core and shell; ensemble effects are caused by the adsorption of molecules on the metal surface due to the existence of distinct atomic groups; geometric effects originate from the different reactivity of the surface atoms [23].

1.1 Objective

The present thesis treats two different catalyst systems for prototypical CO oxidation: the alumina-supported Au@Pd core@shell nanoparticle system and highly dispersed Pd and Pt onto CeO_2. The goal is to achieve a more profound understanding of design principles for enhanced catalytic activity.

2 Background

2.1 Heterogeneous catalysis

2.1.1 Basic concepts

Catalysis is a phenomenon that affects the chemical reaction rates, and a catalyst is a material that changes the pathway of a chemical reaction without being consumed [24]. Catalysis at the interface is called heterogeneous catalysis and is widely used in chemical, refinery and pollution-control processes [25]. Generally, in heterogeneous catalysis, solids catalyze molecular reactions in gas or liquid phases [26]. For the solid catalyst, the active components are usually in low concentrations and are often immobilized in a dispersed form on support materials [1]. The catalytic reactions usually happen on a solid surface with many catalytic sites unless the solids are microporous hosting single sites. Every catalytic reaction is a sequence of elementary steps, where the reactants bind to the catalyst surface and react. The obtained products then detach and liberate the surface for the next catalytic cycle [26]. In order to visualize how a catalyst accelerates chemical reactions, a potential energy diagram can be used as in Figure 2.1 (reproduced from [26]). Here A and B are reactants, while C is the product. The reactants and products are in the gas phase, and the catalyst is in the solid phase.

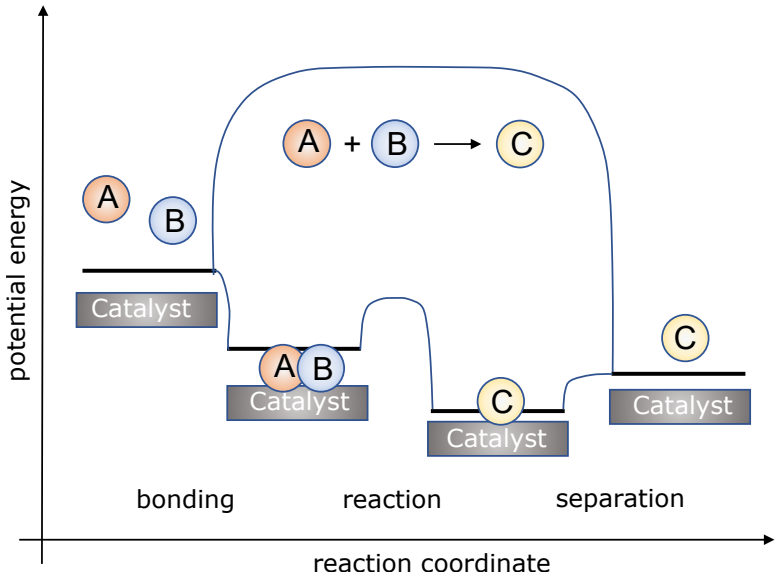

Figure 2.1: *Potential diagram of heterogeneous catalytic reaction*

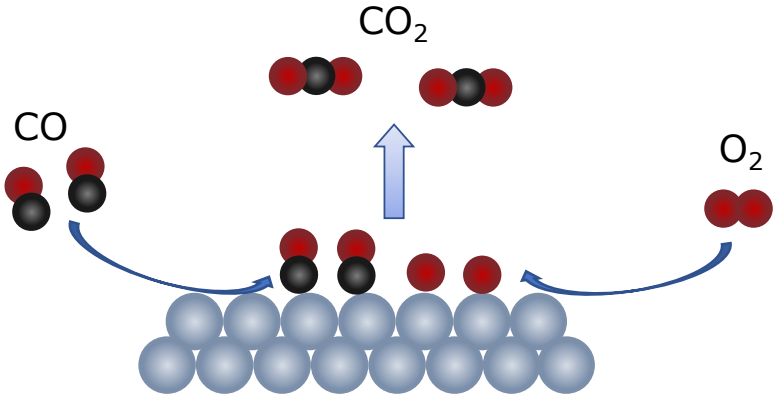

Figure 2.2: *An example of a reaction mechanism of CO oxidation over a noble metal surface*

For a non-catalyzed reaction, the reaction pathway simply involves the collision of A and B with sufficient energy to overcome the activation energy barrier. The catalyzed reaction usually starts from the binding of reactants onto the catalyst surface, which is exothermic, and the free energy is lowered. Then A and B react on the surface. This process is associated with an activation energy, which is much lower than the energy barrier in non-catalyzed reactions. Finally, product C detaches from the catalyst in an endothermic step [26].

An introductory example to explain the catalytic process or catalytic cycle can be the catalytic oxidation of CO on a noble metal surface, such as platinum or palladium. To start with, we assume that metal surfaces are a collection of active sites. The definition of active sites was first brought up by Taylor in 1925. He suggested that the active sites make up the small fraction of the catalyst surface that is catalytically active and usually consist of an atom or an ensemble of atoms [27]. To describe the process, the active sites are denoted with '*'. Generally, the catalytic reaction cycle starts with the adsorption of CO and O_2 molecules onto the metal surface, whereby O_2 molecule dissociates into two O_{ads} atoms. Then the adsorbed CO and O atoms react, forming CO_2. Then the CO_2 detach from the catalyst surface. The adsorbed atom or molecule on the metal surface is denoted as M^* (M here represents adsorbed CO and O). The process could be written as follows [26]:

$$O_2 + 2^* \rightleftharpoons 2O^*$$

$$CO + {}^* \rightleftharpoons CO^*$$

$$CO^* + O^* \rightleftharpoons CO_2 + 2^*$$

A general reaction procedure on a catalyst surface is described in Figure 2.2

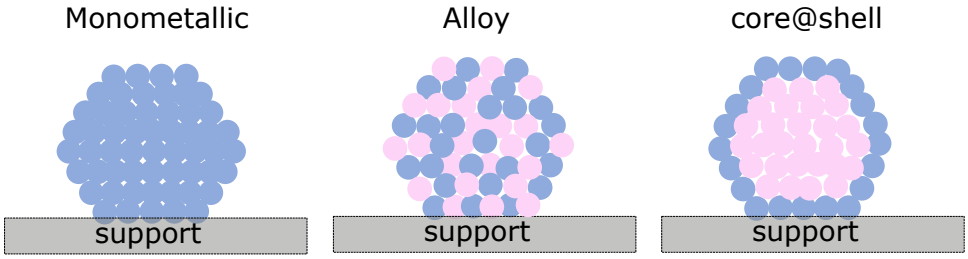

Figure 2.3: *Cross-sections of different types of supported nanoparticle catalysts*

2.1.2 Catalyst design

In most industrial processes, the preferred catalysts are usually in the solid phase that react with the gaseous or liquid reactants, because the solid catalysts are easily separated from the final products [28]. In recent years, supported nanoparticle catalysts have been at the frontier of research, because the transition from microscale to nanoscale will lead to an immense change in both physical and chemical properties of a material [29]. The development of modern synthesis techniques allows diverse shapes of nanoparticles, such as spherical, rod-shaped, cubical, hexagonal, and other shapes [30–32]. Nanoparticles can be categorized into monometallic and bimetallic nanoparticles based on their compositions. Generally, the monometallic nanoparticles are made of a single material, as stated by the name. While the bimetallic nanoparticles consist of two materials different structures are possible (alloy or core@shell, which is a compromising of an inner core material and an outer layer material). A brief structure of both monometallic and bimetallic nanoparticle catalysts are shown in Figure 2.3.

2.2 Applications of supported monometallic catalysts

Supported noble metal catalysts are playing important roles in the industry for several reactions, and offer venues for different heterogeneous catalytic reactions [33, 34]. Among them, supported monometallic catalysts and bimetallic catalysts are of great interest.

2.2.1 Traditional monometallic catalysts

Traditional supported monometallic catalysts are usually very small noble metal particles supported on refractory supports, which provide high surface area [33], and they are used in many industrial applications. For example, total oxidation of methane[35–43], hydrocarbon oxidation, [44, 45] and low temperature CO oxidation [46–51].

In the beginning, the supporting materials are usually inert and their primary role is to enhance the stability of small particles through anchoring [33]. Later, in the 1970s, the term 'metal-support interaction (MSI)' was introduced and the potentials of the active supporting materials were investigated using model catalysts [52]. In the field of catalysis, metal oxides are the most applied supporting materials due to the possibility of tuning the catalytic activity [53], and can be classified into two categories: non-reducible metal oxides and reducible metal oxides. The difference between these two categories is the different ability to create oxygen vacancies as the reaction center, as well as the oxygen storage ability [53].

The most often used non-reducible metal oxides are non-transition metal oxides. For example, La_2O_3, SiO_2, and Al_2O_3 etc. Especially, γ-Al_2O_3, has received substantial research interest because of its high specific surface area and low cost [42, 54, 55]. Metal oxides, such as CeO_2, TiO_2, and zeolites, have also been widely investigated as they could participate in the catalytic reactions and induce strong metal-support interaction (MSI) that can promote catalytic conversions [49, 52, 56, 57]. These include providing the specific adsorption site, enabling electron transfer, and providing additional acidity or basicity to the catalysts [33]. All of those factors have the possibility to strongly affect the catalytic properties of supported metal catalysts, especially supported nanoparticle catalysts [33].

2.2.2 Promotion by active supports

It is challenging but desired to decode the underlying mechanisms and the promoting effects of catalyst-support interactions on catalytic reactions because it provides the opportunity to tailor and moderate catalytic properties via the deliberate choice of included elements [49]. The role of the support is rather complicated and not fully understood in some cases [33]. A general consensus is that in the metal-support system, the role of support is not only simply providing high metal dispersion, but rather a synergy of other important effects [52]. First of all, the support itself may expose active sites for catalytic reactions [58]. Particularly, in some cases, the metal-support boundary seems to provide, predominantly, the active sites [53, 59]. Moreover, particular oxygen atoms from the support can transfer to the reactants, providing oxygen vacancies that can promote desired reactions, and the ambient oxygen will refill the vacancies to restore the original metal-oxide stoichiometry [58, 60].

In addition to providing oxygen vacancies as active sites for direct participation in the reaction, there are several other factors that affect the catalytic activity [53]. Metal-support interactions (MSI) (shown in Figure 2.4, where each blue sphere is one metal atom, and the whole blue part represent a metal nanoparticle, and the metal-support interactions occur at the interface between metal particles and the supporting materials) that affect the shape and size of the metal nanoparticles, as

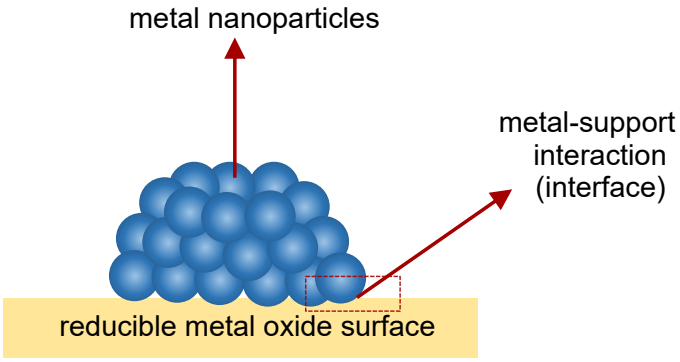

Figure 2.4: *Illustration of metal support interaction*

well as the activation procedure, is of great importance. The smaller the particle size, the more active the sites are [18, 61]; The effect of metal nanoparticle sizes is the consequence of different interface energies, leading to different numbers of low-coordinated atoms [18].

Another factor is the lattice strain either on the support surface or at the interface between metal species and the support, which triggers the variation of electronic and mechanical properties of metal species [62]. The interatomic strain is usually negatively related to the particle size [63].

Besides, charge transfer between small metal clusters and the substrates, in which defect sites (vacancies, holes, etc.) that are essential to the catalytic activity and selectivity are created [58].

2.3 Applications of supported bimetallic catalysts

Besides involving active support, introducing a second metal is also regarded as an effective way to enhance catalytic activity. Compared to the corresponding monometallic catalysts, bimetallic catalyst systems can exhibit superior performances [64].

There are two major mechanisms accounting for the variation of chemical property, namely strain effects and ligand effects [65]. A sketch of the strain effect is shown in Figure 2.5, where ε_f is the Fermi level, ε_d is the d-band center. The strain effect is generated by lattice mismatch, which alters the adsorption energy of the surface atom by changing the d-band center through the long-range effect, even when the surface is more than a few atomic layers away from the strain source [66, 67]. It occurs in solid alloy systems wherein metals with different lattice parameters are joined together, or in core@shell systems where the shell metal possesses different lattice parameters from the underlying core metal [66]. The surface adsorption energy is affected by binding strength, which can be explained by the alteration of electron structure during the adsorption process of the reactants onto the metal surface. During adsorption, the valence state of

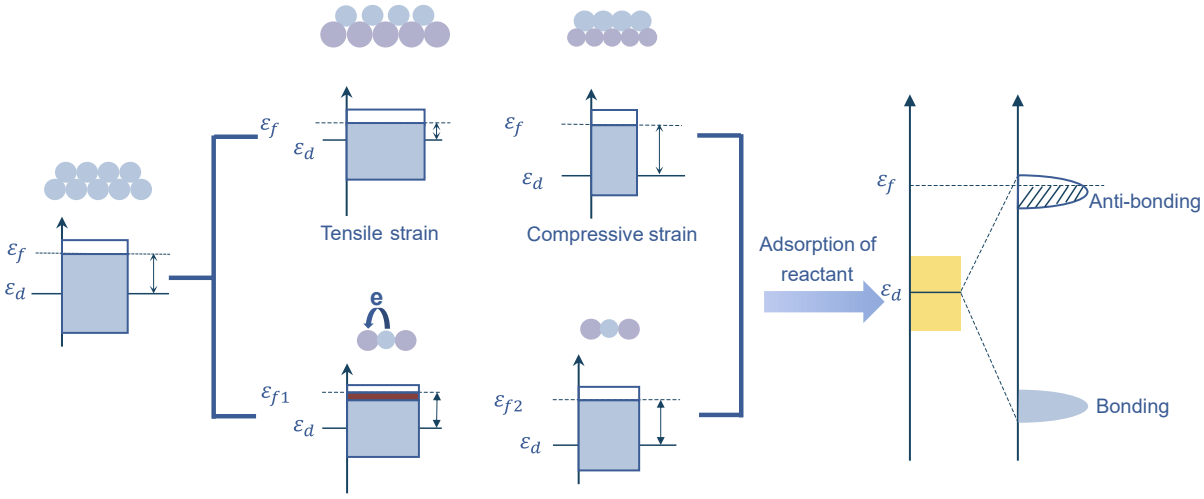

Figure 2.5: *d-band theory and strain effect*

the adsorbate first couples with the s-state of surface metal atoms, then turns to couple with metal d-states, leading to the separation of d-states into bonding and anti-bonding states [68–70]. The binding strength between an adsorbate and a surface metal atom will increase with the filling of bonding d-states or unfilling of anti-bonding states, and the occupancy of the anti-bonding states is only affected by their relative locations to the Fermi level [68, 69]. When the tensile strain happens, the overlapping of d-orbitals will decrease, resulting in a narrower d-band and an up-shift of the d-band center (closer to the Fermi level). The bonding state is always filled because they are far below the Fermi level, while the filling degree of the anti-bonding state depends on its relative energy level to the Fermi level, and largely contributes to the binding ability of molecules on the metal surface. An up-shift of the d-band center relative to the Fermi level leads to less anti-bonding filling and higher energy, then a stronger bond formation. While the downshift of the d-band will cause more filling of anti-bonding orbitals and weaker bond formation.

The ligand effect arises when the coordination condition of a metal atom changes, involving charge transfer and orbital hybridization of metals, leading to the formation of hetero-nuclear metal-metal bonds [71]. However, the strain and ligand effects always occur simultaneously, and it is not straightforward to separate the individual effects. Experimentally observed effects are usually the sum of the two [72]. The combination of strain and ligand effects is always used for the tuning of chemical properties of the surface, potentially resulting in the enhancement of surface reactivity and/or catalytic activity. One of the most common ways of introducing lattice strain into nanoparticles is adding the second metal, forming either alloy or core@shell system [73].

2.3.1 Alloyed nanoparticles

The definition of alloy nanoparticles is not always consistent in the literature. Ponec and co-authors [74] defined alloy as a metallic system containing two or more metal components, irrespective of their degree and mode of mixing [74]. The alloys defined in this way could form either a continuous monophasic alloys, or segregate into biphasic alloys under certain conditions (for example with temperature [74]). However, Zafeiratios *et al.* described the alloy as a chemical compound of two or more metallic parts that adopt at least partly to an ordered crystal structure differing from their corresponding constituent metals [75]. To clarify, in this thesis, an alloyed system is regarded as a bimetallic system in which two different metals are joined together to form an ordered crystal structure. In bimetallic alloy systems, the strain and ligand effects are caused by a size mismatch in the fcc random alloy and the redistribution of noble metal 5d states in the form of intermetallic interaction [76].

The enhancement of catalytic activity caused by strain and ligand effects in alloyed systems has been widely studied, especially in the treatment of vehicle emissions [77–79]. Xu and co-authors have studied the low-temperature CO oxidation over a composition series of silica-supported Au-Pd alloys. The mixture of 72.5% Pd_90Au_10 and 27.5% Pd_31Au_69 was active at 300 K and more stable than bulk Au [80]. Hu *et al.* investigated the methane oxidation over alumina-supported Pd-Pt alloy catalyst in a high humidity feed, and figured out the aging process could change the catalyst structure without sintering of Pd and Pt nanoparticles. Moreover, the active Pd oxidized state was also maintained [81]. Liu *et al.* also studied the synergism of Fe and Pt Species for low temperature CO Oxidation, they found enhanced catalytic activity was due to the contribution of Fe species to O_2 activation [82]. Koutsopoulos and co-authors have synthesized glass silica supported Pt and Pt alloy catalysts, and used them for sulfur dioxide oxidation. The results showed Pt-Pd alloy had a significant enhancement of conversion compared to the Pt only catalyst [83].

2.3.2 Core-shell nanoparticles

Another bimetallic structure is the so-called core-shell structure. The terminology 'core-shell' (in this thesis denoted as 'core@shell') can be broadly defined as a combination of a core (inner) material and a shell (outer layer) material. Among all varieties of core@shell nanoparticles, the concentric spherical core@shell nanoparticles are the most commonly used ones, in which a spherical core particle is partially or entirely coated by a shell of another material [29]. The intrinsic aspect that distinguishes the core@shell system from the alloy system is that the energy bands of the constituting metal elements are overlapping in the alloy system, while this is not the case in the core@shell system [84]. In the core@shell system, when the shell metal atoms are exposed to the underlying core metal,

they usually undergo either tensile strain or compressive strain. The resulting strain in the crystal lattice happens within several atomic layers distance from the interface between the core and the shell and causes lattice distortion [67]. This lattice distortion will lead to a change in the electron structure. Taking Pd as an example. When Pd is used as shell material, and Au is used as core material, the surface Pd atoms will be subjected to tensile strain. In this case, the narrowing of overlapped d states between surrounding metal atoms caused by enlarged interatomic distances will broaden the d-band width of Pd atoms [66]. Moreover, as the d-band of Pd is highly filled ($4d^{10}5s^{0}$), the d-band center will up-shift to a higher level in order to maintain the fixed d occupancy, resulting in an enhanced chemical-adsorption affinity towards some intermediates [66], especially some small adsorbates such as O, H and CO [65]. On the contrary, when the shell atoms are experiencing compressive strain, the d-orbital overlaps will increase, leading to the narrowing of the d-band and lowering of average energy. Correspondingly, the affinity towards simple molecules is lower than those of the parent metal surface [65].

There are many studies on supported transition metal core@shell nanoparticles in the field of catalysis. Zeng *et al.* studied the promotion of Au core in carbon-supported Au@Pt core@shell system for the methanol oxidation reaction. The Au@Pt/C exhibited enhanced activity, and they ascribed this promotion of catalytic activity to the electron exchange between Au and a very thin Pt layer, which provided active oxygen species on Pt and decreased the CO poisoning [85]. Yin and co-authors prepared silica-supported Au@Fe_2O_3 core@shell catalysts and tested their performance in CO oxidation. The obtained catalysts exhibited higher activity comparing to the Au/SiO_2 and Fe_2O_3/SiO_2 catalysts [86]. Li *et al.* performed a comparison study over moisture-treated Pd@CeO_2/Al_2O_3 and Pd/CeO_2/Al_2O_3 catalysts for three-way catalytic (TWC) reactions, and investigated the effect of the core@shell interface. The results showed Pd@CeO_2/Al_2O_3 had better TWC activities compared to the Pd/CeO_2/Al_2O_3 catalysts, which was caused by the excess PdO_2 on the interface between Pd and CeO_2 [87].

Among these supported transition metal core@shell nanoparticles catalysts, supported well-defined Au@Pd core@shell nanoparticles are of great interest. Hosseini *et al.* performed the comparative study of total VOC oxidation over Au@Pd/TiO_2 core@shell, Pd@Au/TiO_2 core@shell and Au-Pd/TiO_2 alloy nanoparticles, and observed higher toluene and propane oxidation activity over Au@Pd/TiO_2 core@shell nanoparticles [88]. Edwards and co-authors studied the direct synthesis of H_2O_2 from H_2 and O_2 over TiO_2 supported Au@Pd core@shell catalyst, and observed enhanced activity compared to Pd and Au only catalysts [89].

2.3.3 Specific objectives

The specific objectives of the present thesis can be divided into synthesis, characterization, catalytic activity studies, and *in situ* DRIFTS studies of the catalysts. The first part focused on the synthesis of alumina-supported Au@Pd core@shell nanoparticles. The effect of synthesis temperature and Pd/Au molar ratio on the morphology of as-prepared nanoparticles was studied. To understand the strain effect during catalytic reactions, Au@Pd with different core/shell ratios, which were denoted as Au5nm@Pd0.5nm, Au5nm@Pd1.5nm, Au13nm@Pd0.5nm and Au13nm@Pd1.5nm, were synthesized. The obtained nanoparticles were loaded onto γ-Al_2O_3 support and used as model catalysts to study the effect of catalyst design on the prototypical CO oxidation reaction. The synthesis method of highly dispersed Pd/CeO_2 and Pt/CeO_2 catalysts was an incipient wetness impregnation.

The morphologies, surface structures, as well as catalytic activities of different samples, were investigated.

3 Methodology

3.1 Materials synthesis

3.1.1 Incipient wetness

Incipient wetness impregnation followed by drying and calcination is one of the most widely used methods for the preparation of heterogeneous catalysts because of its simplicity, low cost and small amount of waste [90]. Generally, for a certain metal catalyst, the corresponding metal salt solutions are used as precursors and simply dissolved in the impregnation solution, and the desired volume is supposed to match the pore volume of the support materials [91]. Commonly used precursors include inorganic metal salts, such as metal sulfates, carbonates, chlorides, nitrates, and organic metal complexes, such as metal acetylacetonates [92]. Water is usually used as the solvent for inorganic salts, while organic solvents are the most commonly used for organometallic precursors [92].

The metal loading is controlled by the concentration of the metal precursor in the solution [91]. To avoid the premature precipitation of metal ions in bulk solution, a concentration below supersaturation is required, which is the amount that is just sufficient to fill the pore volume of the support [92]. The uptake of the liquid into pores of supporting material is caused by the capillary pressure difference Δp across the hemispherical meniscus with a radius of r_p based on the Young-Laplace equation [93]:

$$\Delta p = (2\gamma_{lv}/r_p)\cos\theta \tag{3.1}$$

Where γ_{lv} is the surface tension between the liquid and vapor interface, and θ is the wetting angle between solid and liquid. When the liquid is wetting, θ is $< 90°$, and the water will penetrate the support spontaneously, which is the case between H_2O and most of the oxide supports. When the liquid is non-wetting, θ is $> 90°$, an external pressure is needed to drive the liquid into the pores because the capillary pressure is negative. This can happen for hydrophobic supports such as carbon, for which a less polar solvent like ethanol is more appropriate [93]. The above equation also reveals that the pressure difference is inversely dependent on the pore size, so the liquid is preferentially sucked up by the smallest pores. The liquid filling rate is usually fast and not considered critical for the catalyst synthesis process [92].

3.1.2 Seeded growth

The seeded growth method is one of the most versatile and reliable methods for the controlled synthesis of nanocrystals of different shapes and compositions [94]. In other words, it is possible to tune the shape, size, and component by adjusting growth conditions. A typical seeded-growth method can be divided into two steps: the formation of seed nanoparticles and the subsequent growth in the growth solution, containing metal precursors, reducing agents, and stabilizers [95]. By adding the preformed seeds into the growth solution (or the other way around), the nucleation and growth process could be separated, which makes it possible to isolate parameters that have effects on the nucleation and growth of metal nanoparticles with various morphology [94].

One of the prerequisites for preparing nanoparticles with different shapes in high yields is the control of crystallinity and shape of the seeds [96]. Nobel metal nanocrystals with face-centered cubic lattice exist in several forms, and the most common ones include single-crystalline, singly twinned, icosahedral multiply twinned crystals [94]. Seeds with the same crystal structure can still have different particle shapes and expose different crystal facets. A crucial parameter to obtain exclusively one particular shape is to tightly control the population of the seeds [94]. For example, single-crystalline Au nanorods were synthesized by single-crystalline Au seeds [97]. It is worth to be noted that small seeds offer a better variation in shape control under different growing conditions [98]. Another key parameter that decides whether the seeded-growth is successful or not is the spontaneous nucleation during the growth procedure, which refers to the nucleation of new nanoparticles without benefiting the seeds [94]. When the seeds do not provide sufficient sites for later growth, spontaneous nucleation will occur, and small metal particles that are structurally fluctuating are formed and attached to the seeds forming different sizes and shapes [94]. In addition to the number of seeds, the reduction kinetic also plays an important role in preventing spontaneous nucleation [31]. For example, increasing the temperature while maintaining the number of seeds will accelerate the rate of spontaneous nucleation [31, 99]. Besides reaction temperature, reactant concentrations and reaction addition rate are also factors that influence the reduction kinetic [99, 100].

3.2 Catalyst evaluation

To evaluate the catalytic performance of a catalyst, a chemical flow reactor is commonly used. Depending on the form of the catalyst, either in form of particles in a fixed bed or coated on a monolith, different quartz tube reactors have been used (powder reactor and monolith reactor). For the powder reactor, a vertical tube with an inner diameter of 4 mm was utilized, while for the monolith reactor, a horizontal tube with an inner diameter of 15 mm was used. The amount of

catalyst used in both powder and monolith reactors was around 200 mg. However, for the alumina-supported Au@Pd core@shell samples, the amount obtained in the present synthesis was rather low. Hence, a sample environment reaction cell originally developed for operando X-ray analysis was used [101]. The reaction cell is made of stainless steel and consists of a back and a front plate, a reactor block, and back and front windows. All the compartments were assembled together by screws. 20 mg catalyst was weighted and sieved to the size fraction between 43 and 80 μm. This fraction was then loaded and held in place between two pieces of quartz wool.

The cell temperature was regulated by a thermocouple placed on top of the main body, and the catalyst temperature was monitored by another thermocouple placed in the catalyst bed in the reaction cell. The feed gas composition was controlled by a set of mass flow controllers (Bronkhorst). The composition of effluent gas was measured by a PFEIFFER VACUUM mass spectrometer, following the m/z ratios 28 (CO), 32 (O_2), 40 (Ar) and 44 (CO_2). The total gas flow was set to be 100 mL/min. The inlet gas composition was 0.2 vol.% CO and 5 vol.% O_2, with Ar acting as the carrier gas for the experiment over alumina-supported Au@Pd core@shell system. The CO oxidation experiment was performed in an order of extinction and ignition. The sample cell was first heated up in O_2 to 200 °C at 5 °C/min, then CO gas was introduced and the temperature was kept at 200 °C for another 10 minutes. Then the temperature decreased to 50 °C and dwelled at 50 °C for 10 minutes. The extinction and ignition cycles were repeated three times.

3.3 Materials characterization

3.3.1 Transmission Electron Microscopy (TEM) and High Resolution Transmission Electron Microscopy (HRTEM)

The transmission electron microscope uses a particle beam of electrons to visualize the specimens and generate highly-magnified images. It is a commonly used and powerful technique in the field of nanotechnology and microbiology because the short wavelength of the electron with high energy could pass through the sample and achieve subnanometer resolution. During the image generation procedure, an electron beam passes through the specimen, being absorbed and scattered, and produces contrast and images [102]. TEM is a tool that provides the opportunity for revealing the atom distribution of a nanocrystal structure even when they are passivized with polymers [103]. Nowadays, with the development of modern technics, TEM is not only providing the atomic information of materials, but also chemical information about a single nanocrystal at a spatial resolution of 1 nm or even better [104].

Modern TEM, which is also called High Resolution TEM (HRTEM), is a TEM

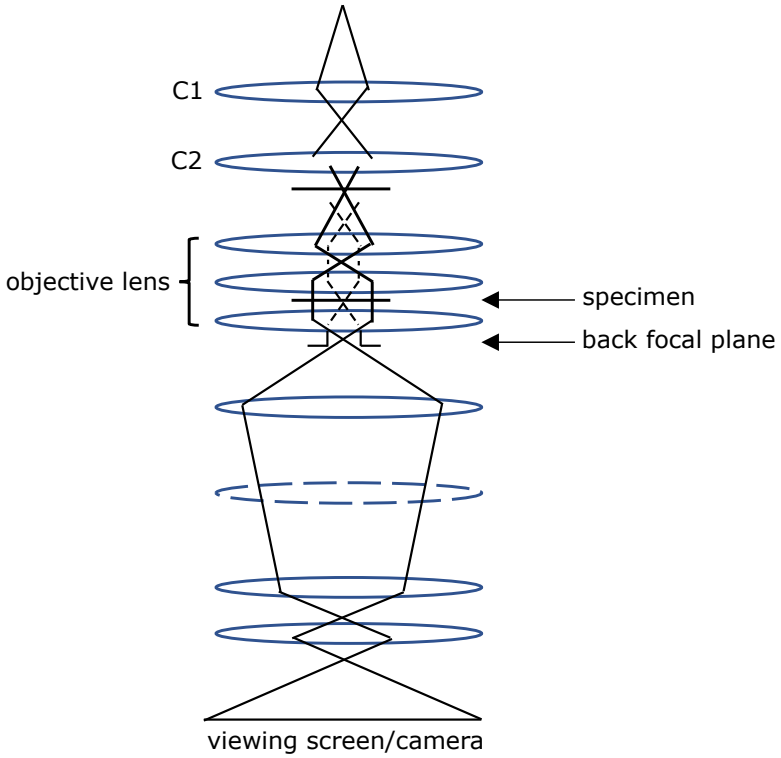

Figure 3.1: *An general optical system in TEM*

consisting of an illumination system, a specimen stage, an objective system, a magnification system, a data recording system, and a chemical analysis system [103]. The electron gun, which uses aLaB_6 thermionic or field emission source as the illumination source, gives high illumination currents and is the center of the illumination system. The LaB_6 gun gives high illumination current, while the field emission source provides higher current density and beam coherence [103]. As a result, the field emission source is unique for performing high-coherence lattice imaging. A schematic of the optical system in TEM is shown in Figure 3.1. When analyzing the structure of a material, the specimen stage is the most essential part, because it gives the opportunity to analyze the physical properties of individual nanostructures [103]. The resolution of the image is determined by the objective lens [103]. The magnification system includes intermediate lenses and projection lenses, giving magnifications of up to 1.5 million. The chemical composition is analyzed with energy-dispersive X-ray spectroscopy (EDS), which is the most precise micro-analysis technique in TEM and depends on counting of X-rays emitted from the beam-illuminated specimen region as a function of the photon energy [105].

The TEM used in the present study is an FEI Tecnai T20 TEM at 200 kV in TEM mode, and FEI Titan 80 - 300 STEM at 300 kV in both TEM and STEM modes. High angle annular dark field scanning transmission electron microscopy (HAADF-STEM) and energy-dispersive X-Ray spectroscopy (EDS) linescan were

used for further indication of core@shell structure.

Specimen preparation

Specimen preparation for Au@Pd core@shell nanoparticles solutions was done by simply adding several drops onto copper-supported holey carbon films. For Al_2O_3 supported nanoparticles, a small amount of sample powder was dispersed in ethanol, the slurry was then drop-casted onto holey carbon film.

3.3.2 X-ray Diffraction (XRD)

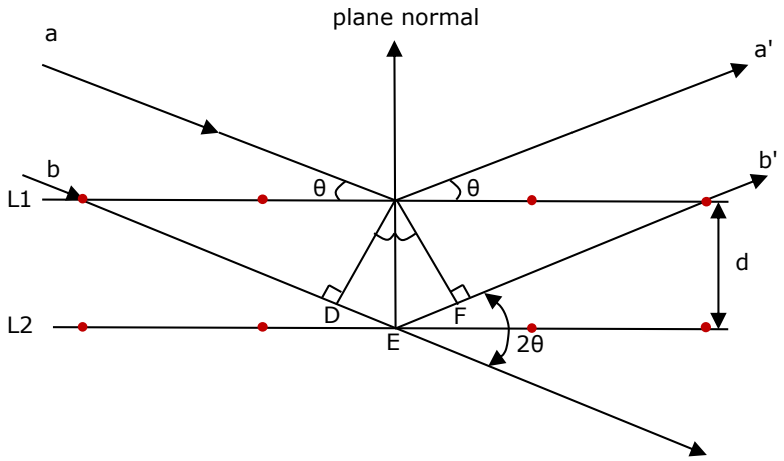

Figure 3.2: *Schematic description of the Bragg reflection of X-rays by a crystal with the interplanar spacing d*

The Powder X-ray diffraction (PXRD) is a bulk-sensitive technique for structural determination [106]. It is used to determine, both qualitatively and quantitatively, the crystalline phases in materials based on their diffraction patterns [106]. It is based on the constructive interference between monochromatic X-rays that a crystalline material can provide. For laboratory instruments, the source of these X-rays is a cathode ray tube. After generation, the X-rays are filtered to be monochromatic, collimated to be concentrated, and directed toward the sample. When the condition fits Bragg's law ($2d\sin\theta = n\lambda$), the incident X-rays would interact with the sample, leading to the production of a constructive interference as well as a diffracted ray. The Bragg's law connects the diffraction angle to the lattice spacing of the crystal phase and the wavelength of electromagnetic radiation, which is described in Figure 3.2. The generated diffracted rays are detected and analyzed. By scanning the sample through a range of 2θ degrees, all the diffraction directions of the sample lattice could be obtained due to random orientation.

XRD measurement

The crystal structure and crystal structure stability of the samples in the present study were characterized by PXRD using a D8 Advance diffractometer (Bruker), with a Cu Kα as the X-ray source and a Lynx-eye energy dispersive detector. PXRD was measured between 20 to 90° under ambient conditions. The incremental step was 0.02° and dwell time was 1.8 s for each step. The sample was loaded onto a capillary sample holder and flattened by a glass slide.

3.3.3 X-ray photoelectron spectroscopy (XPS)

The X-ray photoelectron spectroscopy (XPS) technique is a surface-sensitive method for the analysis of energy distribution of the electrons emitted from X-ray irradiated compounds [107]. Generally, all electrons from the core to the valence levels could be analyzed [107]. The popularity of XPS stems from its ability to identify and quantify the surface elemental composition and to reveal the chemical environments with easy sample preparation [108].

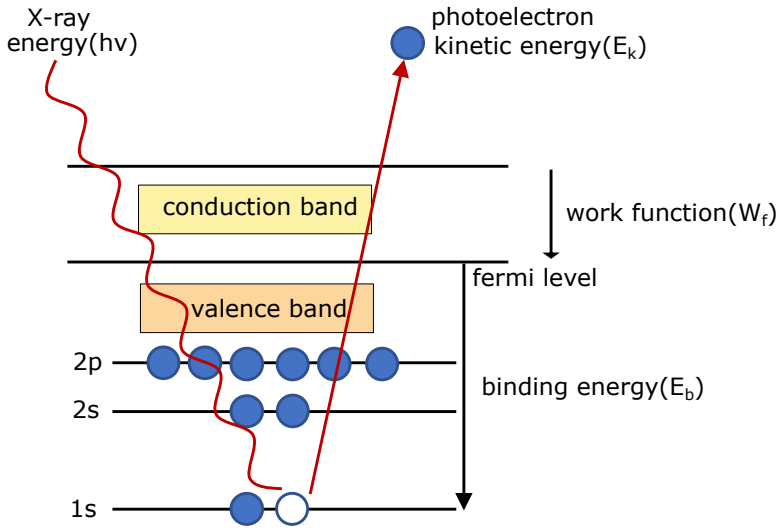

Figure 3.3: *A description of principle for X-ray photoelectron microscopy*

A schematic description of the XPS principle is shown in Figure 3.3. Production of photoelectrons with discrete kinetic energy is described by a single-step process, where an electron initially bound to an atom is ejected by a photon with known energy ($h\nu$) [108]. Since photons are packages of energy that are massless and chargeless, they will undergo complete energy transfer from photon energy to kinetic energy during the photon-electron interaction. If the energy is sufficient, it will lead to the emission of electrons from the atom in the solid. The kinetic energy (E_k) of the emitted electrons is the quantity measured [108]. It is a function of the binding energy (E_b), which is also element and environment specific [108]. Electrons that are undergoing energy losses in traveling the sample can be seen in

the background spectra [108]. The kinetic energy could be expressed in equation 3.2.

$$Eb = hv - Ek - Wf \tag{3.2}$$

XPS measurement

The samples were measured in powder form. The sample powders were mounted on a conduction carbon sticky tape and pumped down for 60 min in the load lock of the vacuum chamber prior to the measurement. X-ray photoelectron spectroscopy data were acquired with a PHI VersaProbe III instrument (Physical Instruments) using monochromated Al-K_α radiation for excitation. An electron flood gun and an Ar^+ ion source were used to facilitate the charge compensation during measurement. The binding energy scale was calibrated to the position of the Al 2p core level at 74.3 eV [109]. For that purpose, the Al 2p signal was fitted with a Voigt profile doublet with a fixed 0.41 eV spin-orbit split [110] and a full width at half maximum (FWHM) of the Lorentzian part of 0.06 eV[111].

3.3.4 X-ray Fluorescence (XRF)

The X-ray fluorescence (XRF) technique is a widely used method for elemental and chemical analysis. The characteristic spectral line radiation emitted by the sample is measured with X-rays to determine the concentration of a certain element [112]. When the materials are exposed to sufficient energy, the energy is absorbed by an atom, the inner shell electrons are excited and transferred to an outer shell, or completely removed. The empty inner shell is then filled with outer shell atoms, leading to the generation of excess energy. The excess energy is emitted as a secondary 'fluorescence' X-ray photon, which has discrete energy corresponding to the energy difference between those two shells. The intensity of the characteristic fluorescence radiation is measured, and it is proportional to the atomic concentration of the corresponding element [113]. An illustration of the XRF principle is displayed in Figure 3.4.

XRF measurement

The X-ray fluorescence spectroscopy used in the present thesis has an Axios spectrometer (Malvern-Panalytical) housing a Rh anode. The samples were measured in loose powder forms in a He atmosphere. The sample was loaded in a polypropylene (PP) sample cup with a 6 mm PP film (ChemPlex) on the bottom. The element quantification was based on calibration with Omnian step samples (Malvern-Panalytical). The software provided by the instrument was SuperQ.

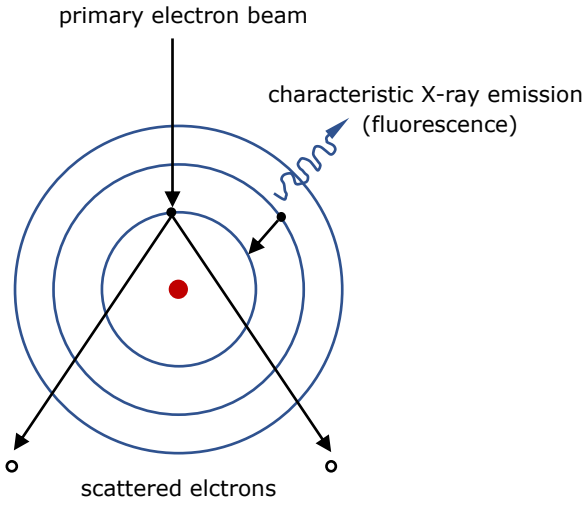

Figure 3.4: *A description of X-ray fluorescence*

3.3.5 Infrared Spectroscopy (IR)

The Infrared spectroscopy (IR) is one of the important techniques for the characterization of catalysts and catalytic reactions. Chemical structural fragments of molecules, also known as functional groups, have the tendency to absorb IR radiation around the same frequency range regardless of the structure of the rest of the environment molecule. This correlation between the molecule structure and the frequency at which it absorbs IR radiation provides the opportunity to identify the structure of unknown molecules and gives the possibility to probe the structural or chemical changes of the molecule [114]. In IR spectroscopy, the characteristic absorption band in the spatial domain is usually expressed in wavenumbers with the unit cm^{-1}. There are two prerequisites for a molecule to be capable of absorbing infrared radiation: it must have specific features; *i.e.* it must possess a change in the electric dipole moment when the bond is vibrating during the vibration of the bond [115]. The vibration involves a change of either bond length (stretch) or bond angle, and the stretch mode includes (in-phase) symmetrical stretches and (out-of-phase) asymmetrical stretches, which depend on the feature of the molecule. [115]. For example, the CO_2 has symmetrical vibration whereas H_2O has asymmetrical vibration. If the molecule has different terminal atoms, the stretching mode will no longer be symmetrical or asymmetrical, but will be a sum up of various proportions of the stretching motion of each group [116]. An example of the H_2O molecule's vibration modes is shown in Figure 3.5. The center of mass is fixed all the time.

The reflection of light could mainly be divided into two categories, termed specular and diffuse reflectance [117]. Specular reflection is an ideal reflection, while diffuse reflectance refers to the reflection of light when radiation hits the material surface before being scattered in many directions instead of only one single angle as in specular reflection. The diffuse reflectance on a solid surface is

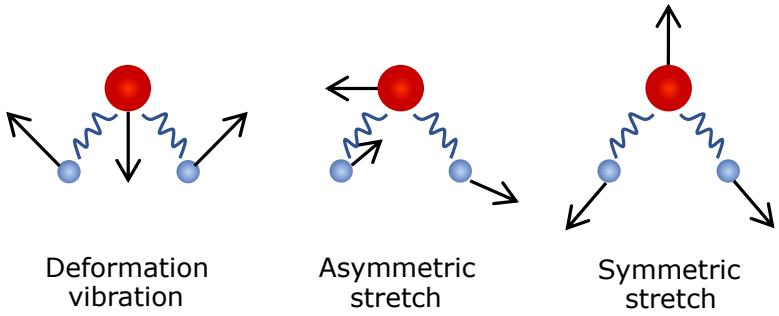

Figure 3.5: *Illustration of the water molecule vibration modes*

caused by both the rough surface and the near surface within a layer [117]. When the incident light enters the material, it is absorbed, scattered, and finally escapes from the material. The light being reflected is recorded, thus the absorption can be obtained. When the light is scattered by materials multiple times, the direction in which it leaves the material is then random [117].

3.4 *In situ* Diffuse Reflectance Infrared Fourier Transform Spectroscopy (DRIFTS)

There are a few modes in which samples could be irradiated. Generally, the reflection can be categorized into three types, which are specular reflectance, attenuated total reflectance and diffuse reflectance [118]. In the present study, diffuse reflectance infrared Fourier transform spectroscopy, which is known as DRIFTS, is used to characterize the surface species during the reaction process, using CO as a probe molecule. The advantage of this technique is easier sample preparation as compared to transmission or specular modes. The sample is usually in powder and acts as its own mirror that allows light penetration. A schematic of the DRIFTS set-up is shown in Figure 3.6.

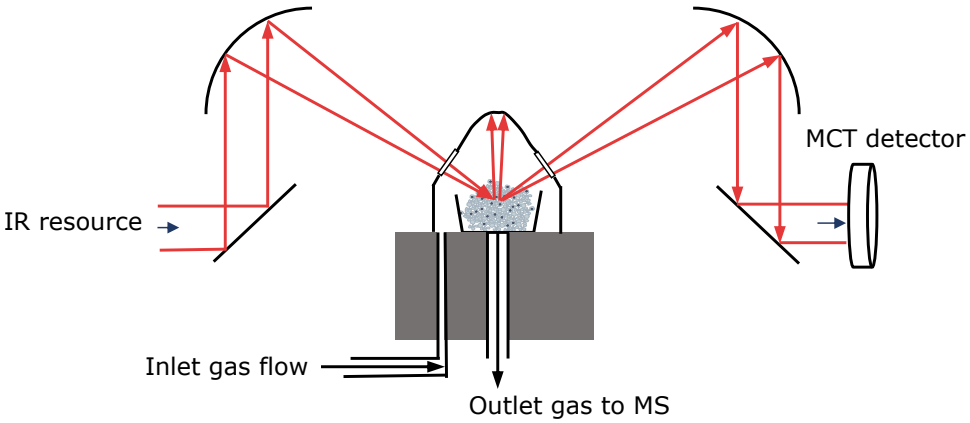

Figure 3.6: *Schematic of* in situ *DRIFTS set up*

In situ DRIFTS measurement

The *In situ* DRIFTS measurements were carried out using an Ultrascan interferometer-based VERTEX 80v FTIR spectrometer (Bruker). A high-temperature stainless steel reaction chamber (Harrick Inc.) with CaF_2 window and liquid nitrogen-cooled MCT detector were used. The temperature underneath the sample holder and inside the sample bed was measured by type K thermocouples. The spectrometer was vacuumed throughout the experiment to avoid the interferences of water vapor or carbon dioxide. The desired feed gas composition was achieved by using individual mass flow controllers (Bronkhorst) for the mixing of gases. Ar (99.9999990%) was used as carrier gas.

The CO adsorption measurements over $Au@Pd/Al_2O_3$ samples were performed over the mixture of $Au@Pd/Al_2O_3$ and 75 mg KBr, which were then loaded in the bottom of sample bed. The sample was first pretreated in 3 vol.% O_2 at 198 °C for 20 min, and then reduced in 3 vol.% H_2 for 1 h using a total constant flow of 100 mL/min. During the exposure to CO, spectra were collected in the range of 400 - 4000 cm^{-1} with a resolution of 1 cm^{-1} during step-wised decreased temperature, ranging from 198 °C to 36 °C, for which individual background spectrum in the presence of H_2 had been recorded. The CO oxidation (ignition) experiment was carried out in the presence of 0.2 vol.% CO and 1 vol.% O_2. The spectra for the ignition process were taken under step-wise ascending temperature from 36 °C to 198 °C.

The Pd/CeO_2 sample was also pretreated in 3 vol.% O_2 first for 40 min, followed by H_2 treatment for 30 min. Unlike experiments for $Au@Pd/Al_2O_3$ samples, the background spectra for Pd/CeO_2 sample were taken under Ar atmosphere. The operated temperature series and the gas composition were the same as for $Au@Pd/Al_2O_3$ samples.

The composition of effluent gas was measured by a PFEIFFER VACUUM mass spectrometer, following the m/e ratios 28 (CO), 32 (O_2), and 44 (CO_2).

4 Catalysts synthesis and *ex-situ* characterizations

Au@Pd core@shell nanoparticles were synthesized by a two-step seeded growth method based on the work by Pella *et al.*[119] and Hu *et al.*[120] although with some modifications. For the large Au@Pd core@shell nanoparticles, the Au core nanoparticles (used as seeds) were synthesized through reduction and nucleation. A general description of the seeded-growth method is described in Figure 4.1.

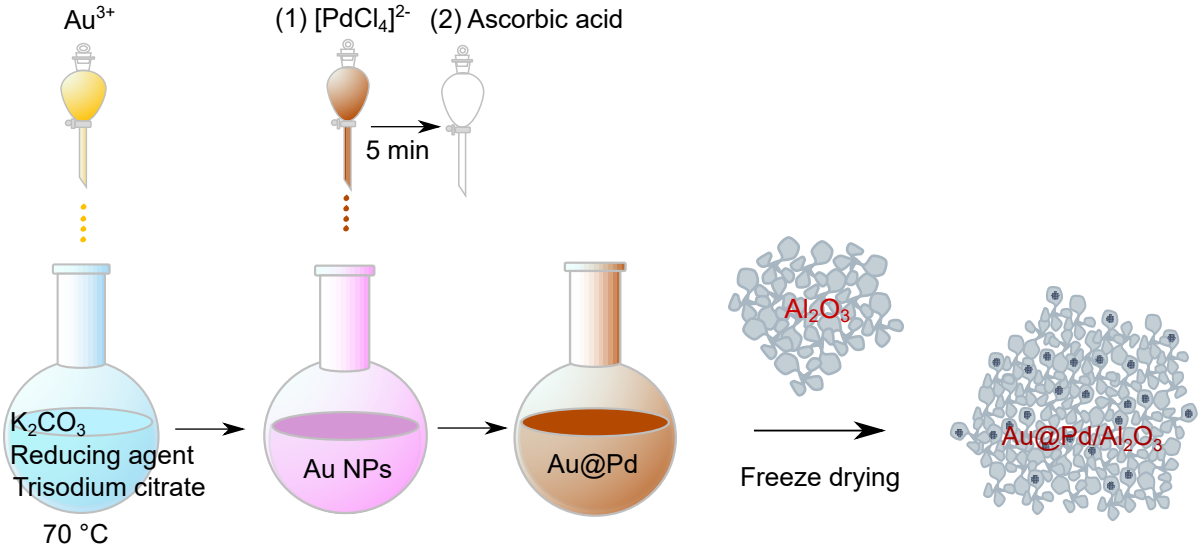

Figure 4.1: *Graphical description of synthesis of $Au@Pd/Al_2O_3$ nanoparticles*

150 mL sodium citrate solution was mixed with 3 mL L-ascorbic acid and 1 mL K_2CO_3 under vigorous stirring and continuous heating. When the temperature reached 70 °C, 1 mL 25 mM $HAuCl_4$ was injected. The color of the solution changed immediately to dark red, indicating the formation of Au nanoparticles [119]. To obtain the Au@Pd core@shell nanoparticles, 0.25 mL H_2PdCl_4 precursor solutions were added into 50 mL as-prepared Au nanoparticles solution, the freshly prepared L-ascorbic acid was added dropwise into the solution. The color of reaction solutions changed to dark brown after the addition of L-ascorbic acid, indicating the formation of Au@Pd nanoparticles [120].

As for the systematic synthesis of Au@Pd with different sizes, tannic acid was used instead of L-ascorbic acid due to the higher possibility to produce Au nanoparticles with narrow size distribution. Similar to the previous method,

150 mL sodium citrate solution was mixed with 0.1 mL tannic acid and 1 mL K_2CO_3 under continuous heating and vigorous stirring. When the temperature reached 70 °C, 1 mL 25 mM $HAuCl_4$ was injected. The color of the solution changed immediately to light pink, indicating the formation of Au nanoparticles. The obtained Au nanoparticles were around 5 nm in diameter. To obtain larger Au nanoparticles, the 5 nm Au nanoparticles were used as seeds. Directly after the formation of 5 nm Au nanoparticles, 55 mL of the prepared solution was replaced by the same amount of trisodium citrate solution. After the solution was heated back to 70 °C, two injections of 25 mM $HAuCl_4$ solution were added with a 10 min time interval. This procedure was repeated three times, and the final size of obtained Au nanoparticles was 13 nm. The growth of the Pd shell with different thicknesses was controlled by the amount of used Pd precursor solution. To obtain 0.5 nm Pd shell on 5 nm and 13 nm Au nanoparticles, 0.25 mL and 0.15 mL H_2PdCl_4 solution were used, respectively. For the preparation of 1.5 nm Pd shell on both 5 nm and 13 nm Au nanoparticles, 2 mL and 1.5 mL H_2PdCl_4 solution were used respectively.

To load the Au@Pd core@shell nanoparticles onto alumina support, 0.4 g γ-Al_2O_3 powder was weighted and directly mixed with as-prepared Au@Pd core@shell nanoparticles solutions and stirred overnight at room temperature. The obtained slurry was then centrifuged under 5000 rpm for 10 min and freeze-dried.

4.1 Preparation of core@shell nanoparticles: effect of operational parameters

Among the factors exerting an effect on the morphologies of core@shell nanoparticles, reaction temperature [121] and precursor molar ratios (Pd/Au) [122] are two of the vital parameters that control the growth of core@shell nanoparticles. However, the effects of those two parameters may vary among different systems. As a result, the effect of different operational parameters during synthesis, different reaction temperatures, and Pd/Au molar ratios were investigated as listed in table 4.1. The reaction temperatures used were 1, 20, and 80 °C. The molar ratio of Pd/Au were 0.31, 3.1, 31, and 310, respectively.

Effect of Temperature

A previous study shows that the morphology of core@shell nanoparticles is dependent on the synthesis kinetics, *i.e.* the competition between the surface diffusion rate and the deposition rate of shell atoms, and is sensitive to the synthesis temperature [123]. Hence, to investigate the influence of temperature on the final morphology of Au@Pd core@shell nanoparticles, different temperatures were explored for the synthesis procedure. The morphologies of as-prepared

Table 4.1: *Different operational parameters*

Sample number	Temperature (°C)	Pd/Au molar ratio
1	1	0.31
2	20	0.31
3	80	0.31
4	1	3.1
5	1	31
6	1	310

Au@Pd core@shell nanoparticles were characterized by TEM imaging. The Au@Pd nanoparticles synthesized under 1 °C, 20 °C and 80 °C are shown in Figure 4.2. As can be seen from the results, the obtained core@shell nanoparticles have shells with thicknesses between 1.5 and 2 nm when the temperature was 1 °C. However, when the temperature increased to room temperature (20 °C) or even higher (80 °C), both the thickness and the roughness of the shell increased dramatically.

To understand the underlying reasons, one should be clear about the growth mechanism of core@shell nanoparticles. As previously reported by Tan *et al.* [123], there are mainly two growing routes for core@shell nanoparticles, namely nuclei coalescence, where the shell nanoparticles are first reduced to nanoparticles in the solution and adsorbed onto the as-prepared core nanoparticles; and monomer attachment, where shell atoms deposit onto the surface of core and then being reduced on the core surface [123], leading to epitaxial growth (shown in Figure 4.3). The reaction temperature plays an important role in determining the final morphology of the core@shell nanoparticles because it determines whether the growth is under thermodynamic control or kinetic control [121]. Another study by Tan and co-authors also suggested the same mechanism. By using real-time imaging through *in situ* TEM, the growth mechanism of Au@Pd core@shell

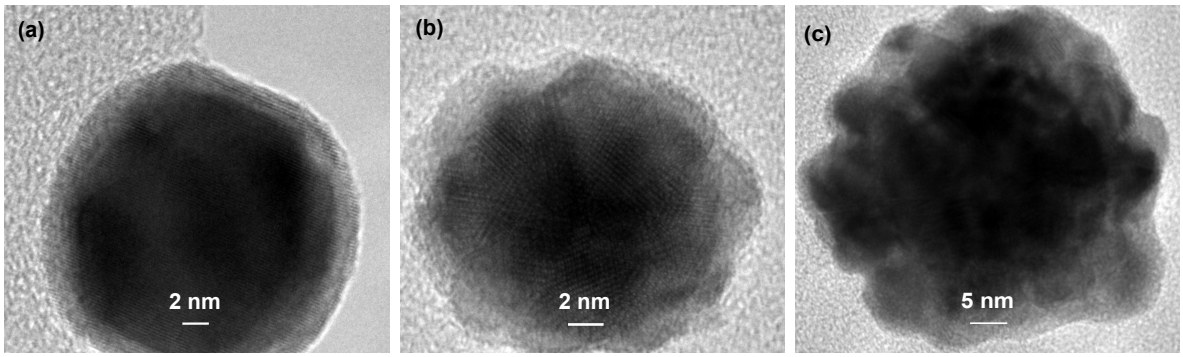

Figure 4.2: *TEM images of Au@Pd nanoparticles synthesized under different temperatures (a)* 1 °C *(b)* 20 °C *(c)* 80 °C

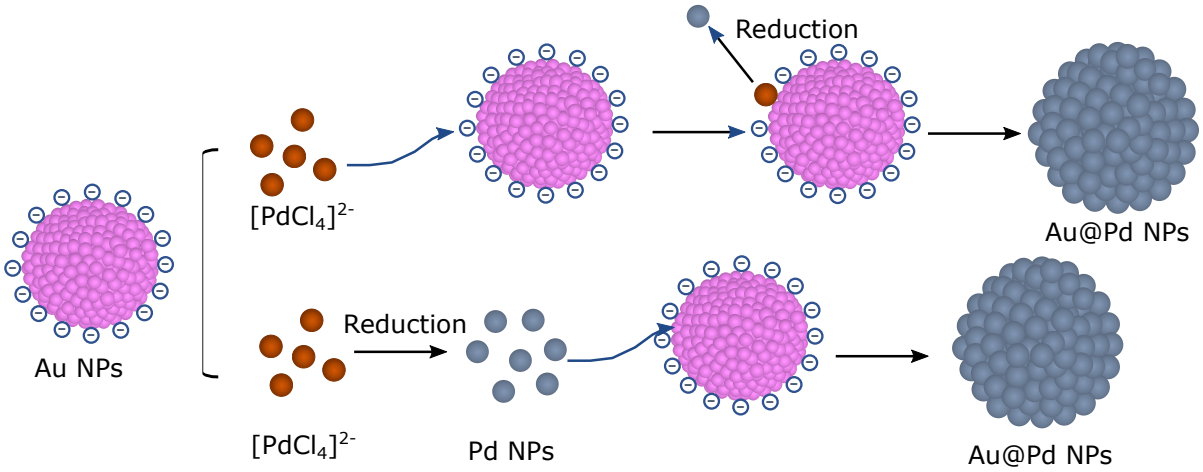

Figure 4.3: *Growth mechanisms for Au@Pd core@shell nanoparticles*

nanoparticles under 20 °C and 80 °C was visualized, and they concluded that under room temperature, the growth is under kinetic control, forming arrow-headed nanorods with thin Pd shells. In contrast, when the temperature increased to 80 °C, the surface diffusion rate was faster, leading to a transfer of the majority of the Pd adatoms from tips to the side facet and the formation of a cuboidal shell [124].

Based on this information, one may propose the following mechanism for the growth of Au@Pd in the present study. In the case of using a temperature of 1 °C, the growth of the Pd shell follows the monomer attachment pathway as the predominant mechanism. The $[PdCl_4]^{2-}$ anion replaces the citrate anion on the Au nanoparticle surface, and the reduction of $[PdCl_4]^{2-}$ to Pd nanoparticles happens on the surface, leading to a thin and evenly distributed shell. This hypothesis is also in accordance with the study from Sarkany *et al.* [125]. However, when the temperature increased to 20 °C and higher (80 °C), the nuclei coalescence became the dominating growth route. In this study, the Pd nanoparticles first formed in the solution, and then deposited onto the Au surface. The deposition rate of the formed Pd nanoparticles is faster than its surface diffusion rate, resulting in rougher and thicker shells.

Effect of Pd/Au molar ratio

Shell thickness, another crucial parameter affecting the catalytic activity of a core@shell catalyst, was controlled by Pd/Au molar ratio in the reaction solution [73]. Hence, the effect of the Pd/Au ratio on the morphology of the as-prepared Au@Pd nanoparticles was investigated by varying the dosage of Pd precursor during Au@Pd synthesis (the reaction temperature was kept at 1 °C). Figure 4.4 shows TEM images of as-prepared Au@Pd nanoparticles synthesized with different Pd/Au ratios, which were 3.1, 31, and 310, respectively. A significant increase

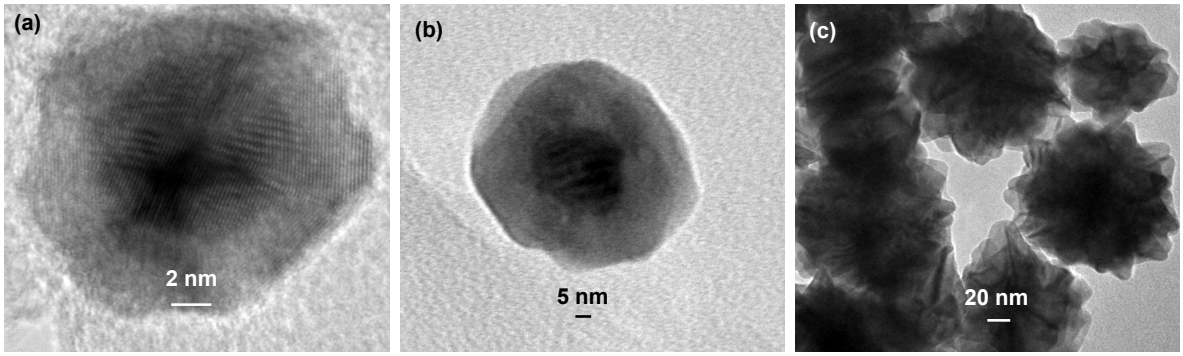

Figure 4.4: *TEM images of Au@Pd core@shell nanoparticles with different Pd/Au molar ratios (a) 3.1 (b) 31 and (c) 310*

in shell thickness and roughness was observed when increasing the Pd/Au molar ratio. This can be caused by the too high availability of Pd in the reaction solution for the growth of the Pd shell on the Au core at a higher Pd/Au ratio. This finding was in accordance with studies from Hu *et al.* [120]. Moreover, when Pd/Au ratio was fairly high (310, see in figure 4.4 (c)), the obtained Au@Pd nanoparticles lost their smooth shell structures and appeared with flower-like morphology. One hypothesis is that when the Pd precursor concentration was too high, the obtained Pd nanoparticles were no longer spherical, but in urchin-like shape due to the fast reaction kinetics. The urchin-like shaped Pd nanoparticles deposited onto the Au surface, leading to flower-shaped Au@Pd nanoparticles [126]. Another hypothesis is that the high Pd concentration disrupted the dispersion of fine Pd nanoparticles, which therefore led to the agglomeration of these nanoparticles. Those agglomerated Pd clusters deposited onto the Au surface, resulting in flower-shaped Au@Pd nanoparticles [127].

4.2 Loading core@shell nanoparticles: structural stability

The composition and configuration of nanoparticles, which influence the defect density at the nanoparticle surfaces [128], have significant effects on the physical and chemical properties of nanoparticles, and therefore their catalytic activities. Consequently, it is of great importance to investigate the structure, as well as crystalline stability of the Au@Pd/Al_2O_3 during the CO oxidation experiment. Figure 4.5 shows TEM images, HAADF-STEM images, and EDS linescan profiles across the surface of the as-prepared Au@Pd/Al_2O_3 nanoparticle catalyst and the same catalyst collected after CO ignition and extinction experiments. The orange lines display the scanning pathways, with the arrows indicating the scanning directions. As can be seen in Figure 4.5 (a) and (c), no notable agglomeration of Au@Pd nanoparticles on Al_2O_3 surface is observed, neither for the loading

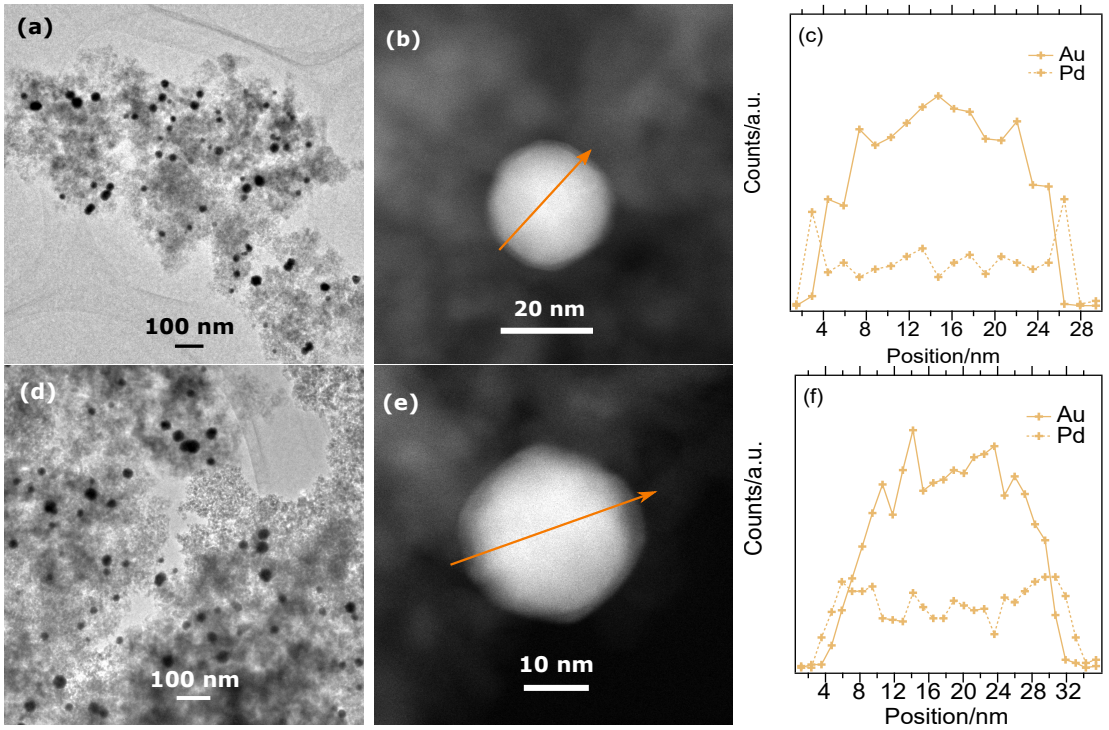

Figure 4.5: *(a) TEM image of as-prepared $Au@Pd/Al_2O_3$ nanoparticles. (b) HAADF-STEM image of as-prepared $Au@Pd/Al_2O_3$ nanoparticles. (c) Linescan profile of $Au@Pd/Al_2O_3$ nanoparticles collected after DRIFTS experiment. (d) TEM image of $Au@Pd/Al_2O_3$ nanoparticles collected after DRIFTS experiment. (e) HAADF-STEM image of as-prepared $Au@Pd/Al_2O_3$ nanoparticles. (f) Linescan profile of $Au@Pd/Al_2O_3$ nanoparticles collected after DRIFTS*

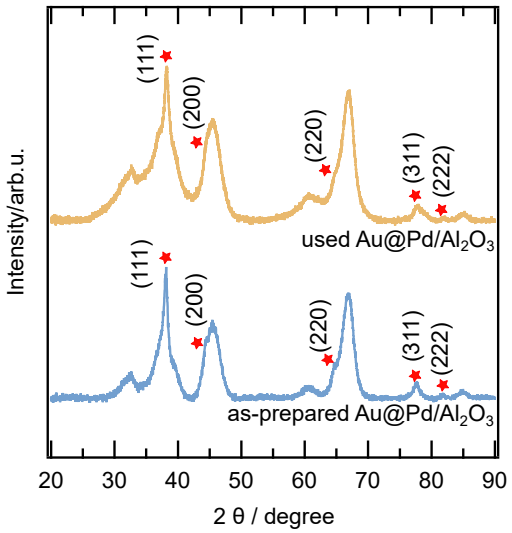

Figure 4.6: *X-ray diffraction patterns of as-prepared $Au@Pd/Al_2O_3$ and used $Au@Pd/Al_2O_3$*

procedure nor the CO oxidation reaction process. Moreover, the HAADF-STEM images in Figure 4.5 (b) and (e), as well as EDS linescan profiles in Figure 4.5 (c) and (f) suggest that the core@shell structure remains upon exposure to CO oxidation condition, indicating good structural stability of Au@Pd/Al_2O_3 core@shell nanoparticle catalyst. Figure 4.6 presents a comparison of the X-ray diffraction patterns for the as-prepared and used Au@Pd/Al_2O_3 samples. In essence, the XRD patterns of the two samples resemble each other, showing the same fcc structure of Au. Moreover, no peaks for Pd or PdO were observed, suggesting that the Pd shell was still thin and intact.

4.3 Synthesis of systematic variations of Au@Pd

In a bimetallic system, strain and ligand effects are known to co-exist and co-impact the reactivity [68]. However, studies that clearly separate the strain effect from the ligand effect during thermal catalytic reactions are still scarce [68, 129]. In light of this, a study that isolates the strain effect was performed. An Au@Pd/Al_2O_3 model catalyst system with a systematic variation of core sizes and shell thicknesses was prepared. Catalysts with 5 nm Au cores with 0.5 nm and 1.5 nm Pd shells, and 13 nm Au cores with 0.5 nm and 1.5 nm Pd shells were prepared, and denoted as Au5@Pd0.5, Au5@Pd1.5, Au13@Pd0.5 and Au13@Pd1.5.

Figure 4.7 shows high-resolution TEM (HRTEM) images of the four as-prepared samples. The lattice distance of the Pd shell and Au core for each sample were measured. For Au cores, the measured lattice distances were 0.23 nm, 0.20(3) nm, 0.23(5) nm and 0.23(7) nm, respectively. The measured lattice distances for Pd shell were 0.19 nm, 0.19 nm, 0.19(6) nm and 0.21(2) nm, respectively. The HAADF-STEM images as well as EDX linescan profiles can be found in Paper II. The average sizes of Au@Pd core@shell nanoparticles were 6.0 ± 0.5 nm, 8.0 ± 0.5 nm, 14.0 ± 0.5 nm and 16.5 ± 0.5 nm. The average thickness of the Pd shell on the Au surface was around 0.5 nm and 1.5 nm, with 0.1 - 0.2 nm deviation. Although the shell thickness was not perfectly mono-dispersed for individual

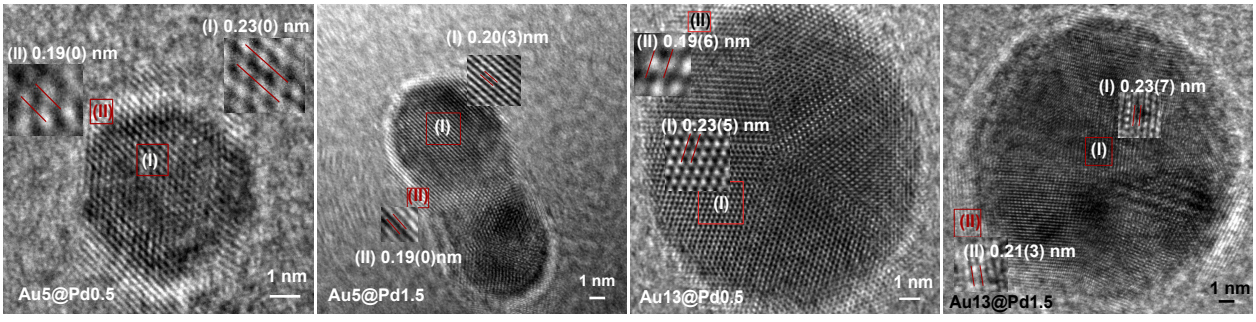

Figure 4.7: *HRTEM images of as-prepared Au@Pd nanoparticles*

particles, the average thickness met the requirement.

Figure 4.8 shows the TEM images of as-prepared Au@Pd/Al_2O_3 samples. The majority of the particles are well dispersed on the alumina surface without significant agglomeration, which is in line with Paper I [99].

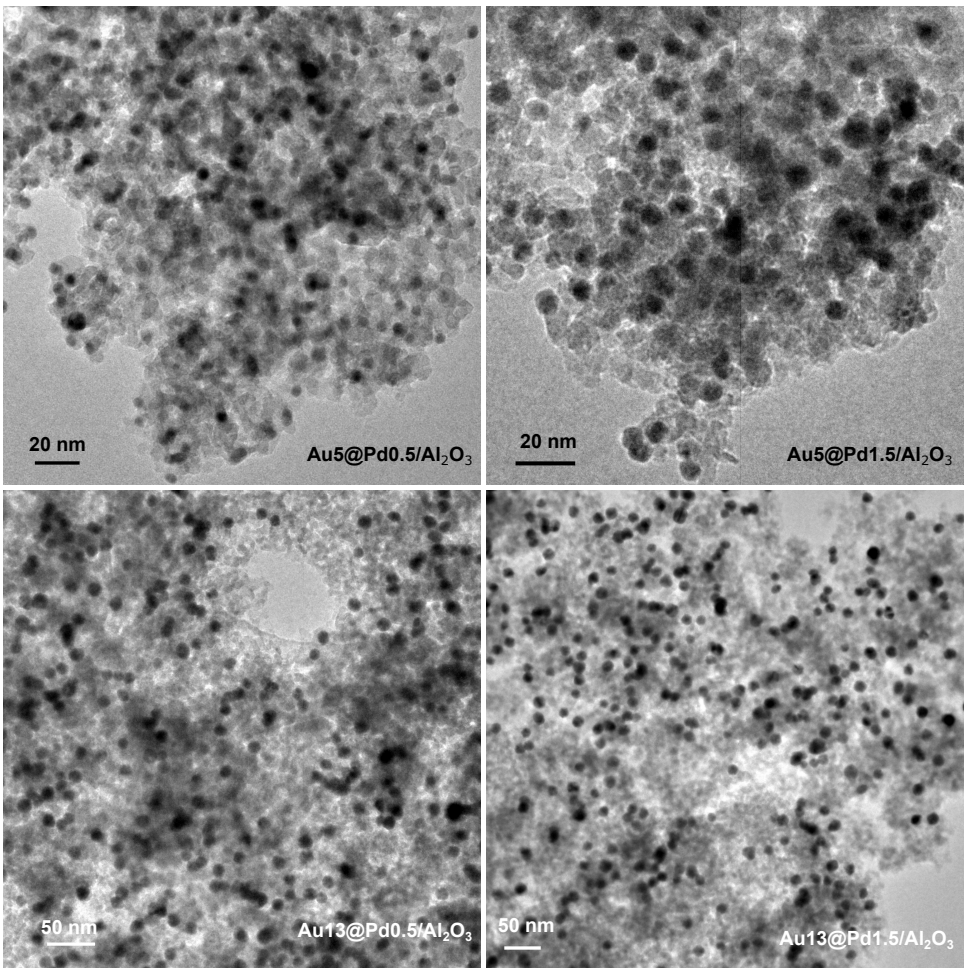

Figure 4.8: *TEM images of alumina supported Au@Pd core@shell nanoparticles with different sizes*

4.4 Elemental composition of alumina supported Au@Pd core@shell

The element compositions of $Au@Pd/Al_2O_3$ with different sizes were measured by XRF. The obtained data are shown in Table 4.2. The Pd loading of four samples was 0.481%, 3.01%, 0.245%, and 1.342%, respectively. The atomic Pd/Au ratios for the four samples were 0.22, 1.89, 0.08, and 0.53, respectively.

Table 4.2: *XRF measurements of as-prepared catalysts*

Elements	$Au_5@Pd_{0.5}$	$Au_5@Pd_{1.5}$	$Au_{13}@Pd_{0.5}$	$Au_{13}@Pd_{1.5}$
Pd	0.481	3.010	0.245	1.342
Au	4.509	2.959	5.442	4.688
Atomic Pd/Au ratio	0.22	1.89	0.08	0.53

4.5 XPS analysis

Figure 4.9 shows the core level Au 4d and Pd 3d region of the XPS spectra of four as-prepared samples. The main results suggest that the signal for PdO with a component at 337.3 eV and 336.8 eV for Au core could only be observed for the sample with 1.5 nm Pd shell, while for samples with a 0.5 nm Pd shell, only metallic Pd signal was observed. This indicates that the Au core has a larger effect on the thin Pd shell, and makes it more difficult for the thin Pd shell to be oxidized. Additional information that can be extracted from the $Au4d_{5/2}$ signal was the average Pd shell thickness. A rough approximation assuming a flat surface and a metallic and homogeneous metallic Pd overlayer was made. The inelastic mean free path (IMFP) of $Au4d_{5/2}$ photoelectrons passing through Pd metal was determined to be 15.5 Å [130]. The estimation of Pd overlayer thickness d could be described in the equation below:

$$d = \lambda_{Au} \cdot \cos\theta \cdot \ln\left(\frac{I_{Au}}{I_{Au+Pd}}\right) \tag{4.1}$$

The IMFP is represented by λ_{Au}, and the measured integral intensity of the $Au4d_{5/2}$ signals as I_{Au} for the bare gold and I_{Au+Pd} for the covered gold, respectively. The Au signal was normalized to the Au loading determined by XRF measurements. The emission angle θ was considered not to significantly affect the signal of spherical particles, hence the cosine term is ignored (we assume normal emission with θ to be zero). The calculated Pd shell thickness is shown in Table 4.3. The calculated Pd shell thickness of all samples is close to the measured thickness by TEM.

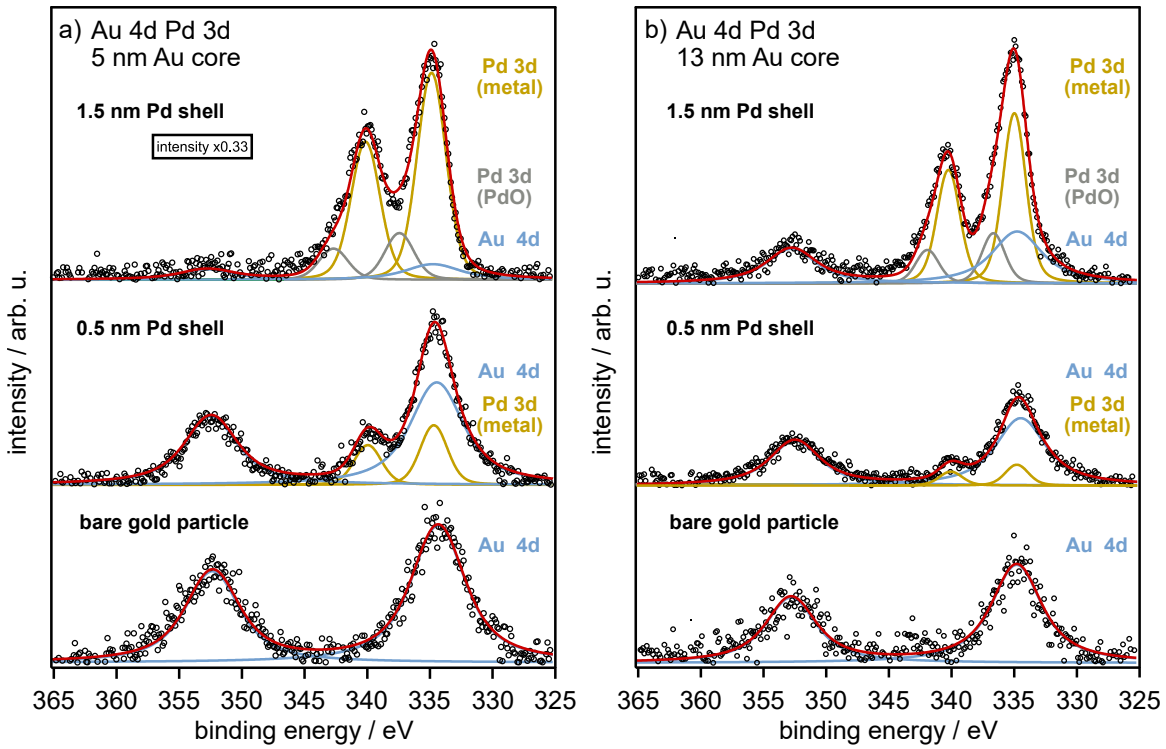

Figure 4.9: *Au 4d and Pd 3d core level XPS spectra of as-prepared Au@Pd/Al_2O_3 samples*

Table 4.3: *Calculated shell thickness based on XPS data*

sample	$Au_5@Pd_{0.5}$	$Au_5@Pd_{1.5}$	$Au_{13}@Pd_{0.5}$	$Au_{13}@Pd_{1.5}$
shell thickness	0.4	1.5	0.8	1.3

5 Catalytic activity and surface properties

5.1 Au@Pd core@shell nanoparticle catalysts

The activities for CO oxidation over the Au@Pd core@shell samples are shown in Figure 5.1. Panel (a) is the CO conversion and panel (b) is the CO_2 concentration over alumina-supported Au@Pd core@shell versus temperature. As can be seen from the results, Au@Pd with 0.5 nm shell thickness exhibit low CO conversion and barely any CO_2 production. The reason could be strong strain effects enhancing the adsorption of CO on Pd surface, leading to strong CO self-poisoning of the Pd surface. However, the Au@Pd catalyst with 1.5 nm shell thickness shows promising CO conversion and CO_2 production. Compared with the alumina-supported Pd catalyst (0.23% Pd and 3% Pd), which starts to produce CO_2 at slightly lower temperatures than the $Au@Pd/Al_2O_3$ catalyst, the CO conversions of core@shell catalysts are promising.

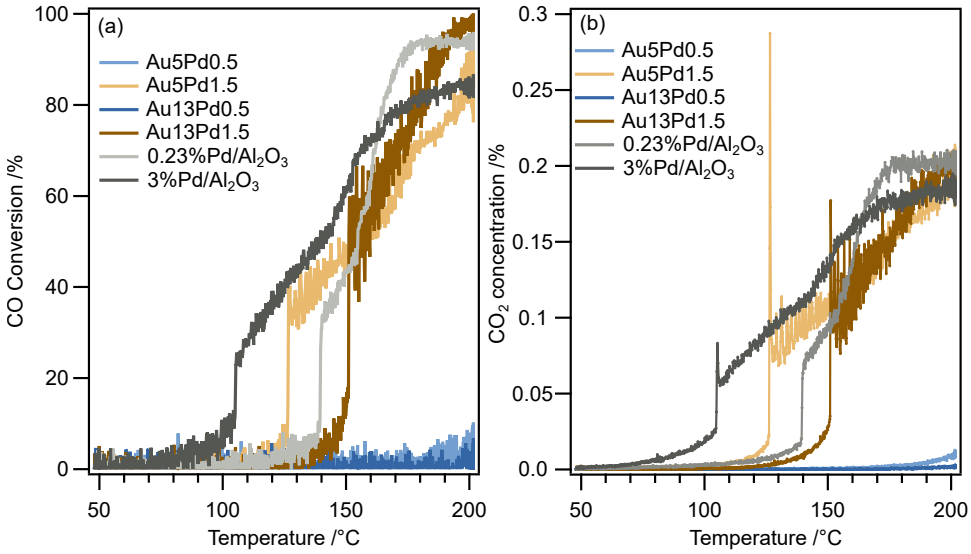

Figure 5.1: *(a) CO conversions vs temperatures; (b) CO_2 concentrations vs temperatures*

To further investigate the underlying mechanism and understand how strain affects the electronic structure of surface Pd atoms, and thus the catalytic properties, the CO adsorption process (from 198 °C to 36 °C) and ignition process

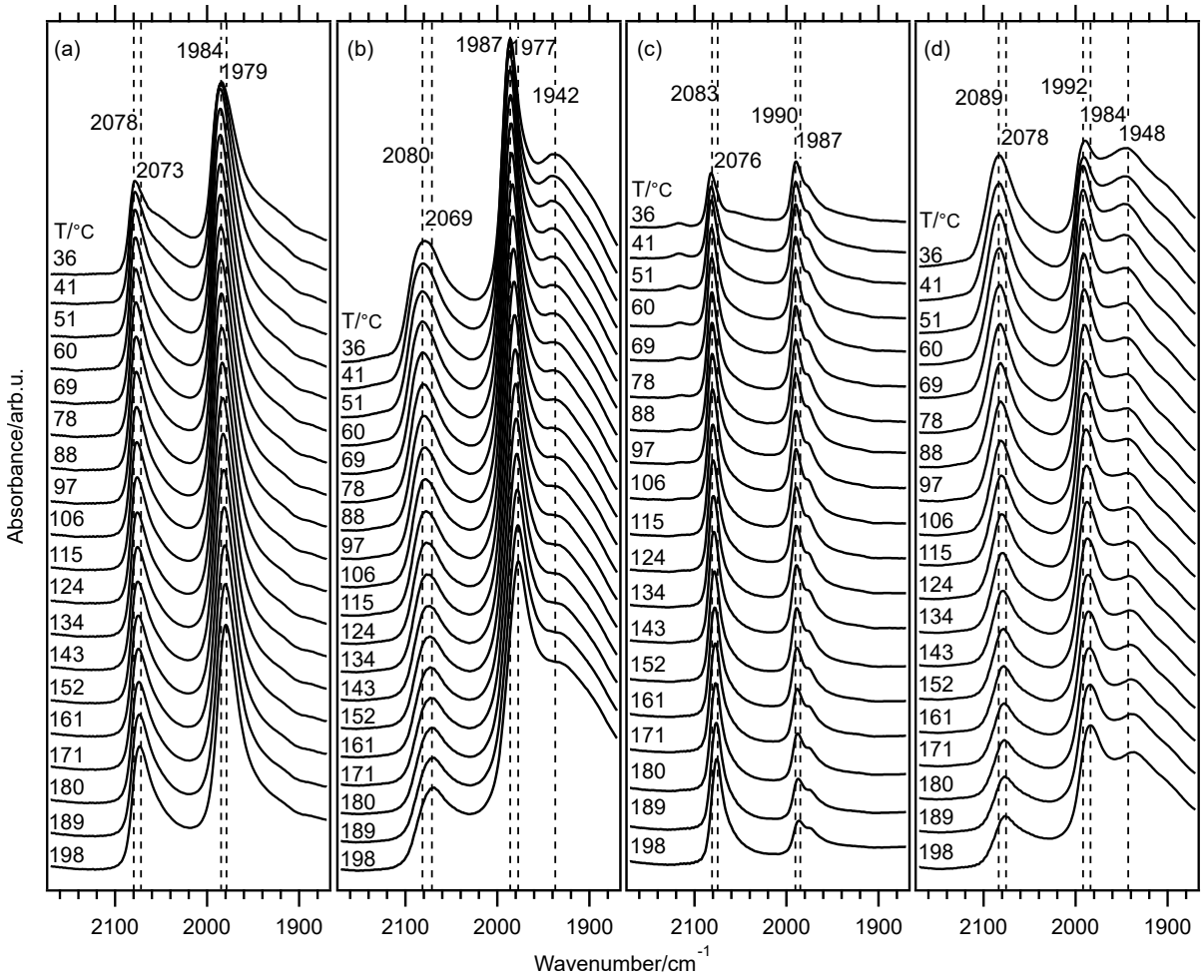

Figure 5.2: *CO adsorption spectra over (a) Au5@Pd0.5/Al_2O_3; (b) Au5@Pd1.5/Al_2O_3; (c) Au13@Pd0.5/Al_2O_3; (d) Au13@Pd1.5/Al_2O_3*

(from 36 °C to 198 °C) on Pd surface were followed using *in situ* DRIFTS. The spectra are shown in Figure 5.2 and Figure 5.3.

Generally, there are three types of adsorbed CO species on the Pd surface: linear bonded CO (2060 - 2085 cm^{-1}), bridge bonded CO (1895 - 2000 cm^{-1}) and three-fold hollow bonded CO (1830 - 1920 cm^{-1}). In the CO adsorption spectra in Figure 5.2, the contribution of gaseous CO was subtracted to make the IR peaks of adsorbed CO species clearer. Upon decreasing the temperature, the IR band for linear bonded CO species blue-shifted 4 cm^{-1} to 7 cm^{-1} for thin-shelled Pd catalysts, while blue-shifted 11 cm^{-1} for thick-shelled Pd catalysts. As for bridge bonded CO species, the IR band blue-shifted around 3 cm^{-1} to 5 cm^{-1} for samples with thin shells, and around 8 cm^{-1} to 10 cm^{-1} for samples with a thick shell. Those blue-shifts indicate higher coverage upon decreasing the temperature and are in accordance with our observation in Paper I, where a CO adsorption study was performed over Au@Pd/Al_2O_3 with around 13 nm Au and 1.5 nm Pd. Considering the peak intensity variation in more detail,

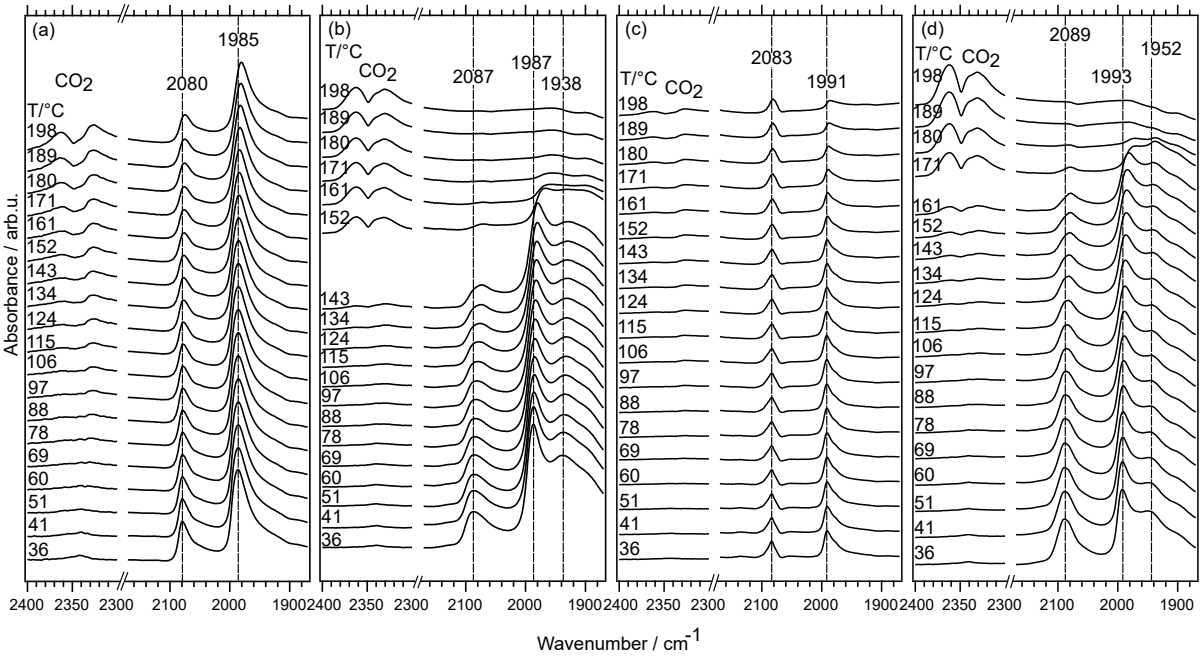

Figure 5.3: *CO ignition spectra over (a) Au5@Pd0.5/Al_2O_3; (b) Au5@Pd1.5/Al_2O_3; (c) Au13@Pd0.5/Al_2O_3; (d) Au13@Pd1.5/Al_2O_3*

both linear bands and bridge bands are stronger at high temperatures and grow less upon cooling for thin-shelled catalysts. However, for the thick-shelled catalyst, the peak intensities of both linear and bridge-bonded CO species are higher at room temperature. This observation suggests stronger binding of CO on thin Pd shells and the surface structure constrains the growth of a dense adsorbate layer more than the thick-shelled samples. The different surface structure between thin and thick-shelled samples is further supported by the fact that the band for linear bonded CO species for thin-shelled samples is sharper than those for the thick-shelled samples at high temperatures. This indicates more well-ordered surface(s) with more distinct adsorption sites. Moreover, the morphology variation among Au@Pd core@shell nanoparticles is smaller for the one with a thin Pd shell than the thick ones, giving rise to the clearer IR band for linear bonded CO.

The IR spectra during the CO oxidation (ignition) process are shown in Figure 5.3. At the beginning of the ignition experiment (36 °C), the Pd surface is covered by CO for all four samples, and the band locations of all peaks slightly shift to higher wavenumbers compared to the adsorption spectra, which could be caused by the presence of O_2. Upon increasing the temperature, the high CO coverage remains stable up to around 130 °C for all samples, reflecting CO self-poisoning. This is in accordance with the reaction cell data, which shows CO conversion at around 130 °C. One should notice that the design of *in situ* DRIFTS and sample environment reaction cell is different, leading to the deviation of the conversion

temperature's correlation. The thick-shelled samples become more active when further increasing the temperature. When the temperature is above 170 °C, the formation of CO_2 gas was observed, indicated by the significant double band at 2350 cm^{-1}. At this temperature, no linear and bridge-bonded CO species could be observed, indicating that all the adsorbed CO have reacted. There is still some adsorbed CO between 140 - 170 °C. However, whether it is due to the partial CO coverage on the particle surface or some particles are covered with CO and some not cannot be unambiguously concluded.

For Au@Pd with a thin Pd shell, there is no significant vanishing of linear and bridged bands upon increasing the temperature. Moreover, the weak intensity of CO_2 gaseous signal under high temperature indicates little formation of CO_2, which is in line with the activity data, where the thin-shelled catalysts are almost inactive. The reason could be that CO binds strongly on the surface Pd sites, which may be affected by the Au core. Apart from the intensity of CO bands, which are related to different particle loading, the general behavior of the two thin-shelled catalysts is similar. Hence, the Au core size can be considered as a secondary effect on the property of the Pd surface. Another reason could be that the CO overlayer leads to a more pronounced blocking effect towards O_2 dissociation. Based on XPS data, the PdO signal could only be observed for thick-shelled catalysts, indicating the difficulty for the thin shell to be oxidized, in other words, it is difficult for the O_2 to dissociate. In this case, CO will only bind on the Pd surface without reacting with adsorbed O species.

5.2 Supported Pd and Pt catalysts

A corresponding study of CO oxidation (extinction) over highly dispersed CeO_2 supported Pd and Pt catalysts was also carried out using *in situ* DRIFTS. Figure 5.4 shows the DRIFTS spectra of gaseous CO_2 region and adsorbed CO region for both Pd/CeO_2 (figure (a)) and Pt/CeO_2 (figure (b)) catalysts during extinction. 3% Pd/Al_2O_3 (figure (c)) is used as a reference.

Starting with the Pd/CeO_2 catalyst: At high temperatures (198 °C), the majority of adsorbed CO species have reacted away, indicated by the intense double band for gaseous CO_2. In spite of maximum CO conversion, some adsorbed CO species are still observed. The band at 2035 cm^{-1} is assigned to the CO linearly adsorbed on Pd^+ and the band at 2073 cm^{-1} and 2094 cm^{-1} are ascribed to linear bonded CO species on Pd^0 surface [131]. The existence of Pd^+ could be due to the effect of the CeO_2 support. Moreover, the band at 2145 cm^{-1} represents gaseous CO species. The band at 1966 cm^{-1} is ascribed to bridge-bonded CO species on Pd^0 surface, which could only be observed at around 134 °C and below, indicating that the adsorbed O species first react with the bridge-bonded CO species. Upon decreasing the temperature, the intensity of the gaseous CO_2 band decreases smoothly, while the intensities for both linearly and bridged adsorbed

CO species increase gradually without a sudden build-up. When the temperature reaches 36 °C, the intensity of adsorbed CO bands reaches a maximum, indicating higher CO coverage. When it comes to Pt/CeO_2 catalyst, a similar trend was observed. The band at 2107 cm^{-1} exists at 211 °C even when the CO conversion is 100%. This band is assigned to CO linearly bonded to ionic platinum. No sudden build-up of adsorbed CO species and vanishing of gaseous CO_2 is observed, which is due to the effect of CeO_2.

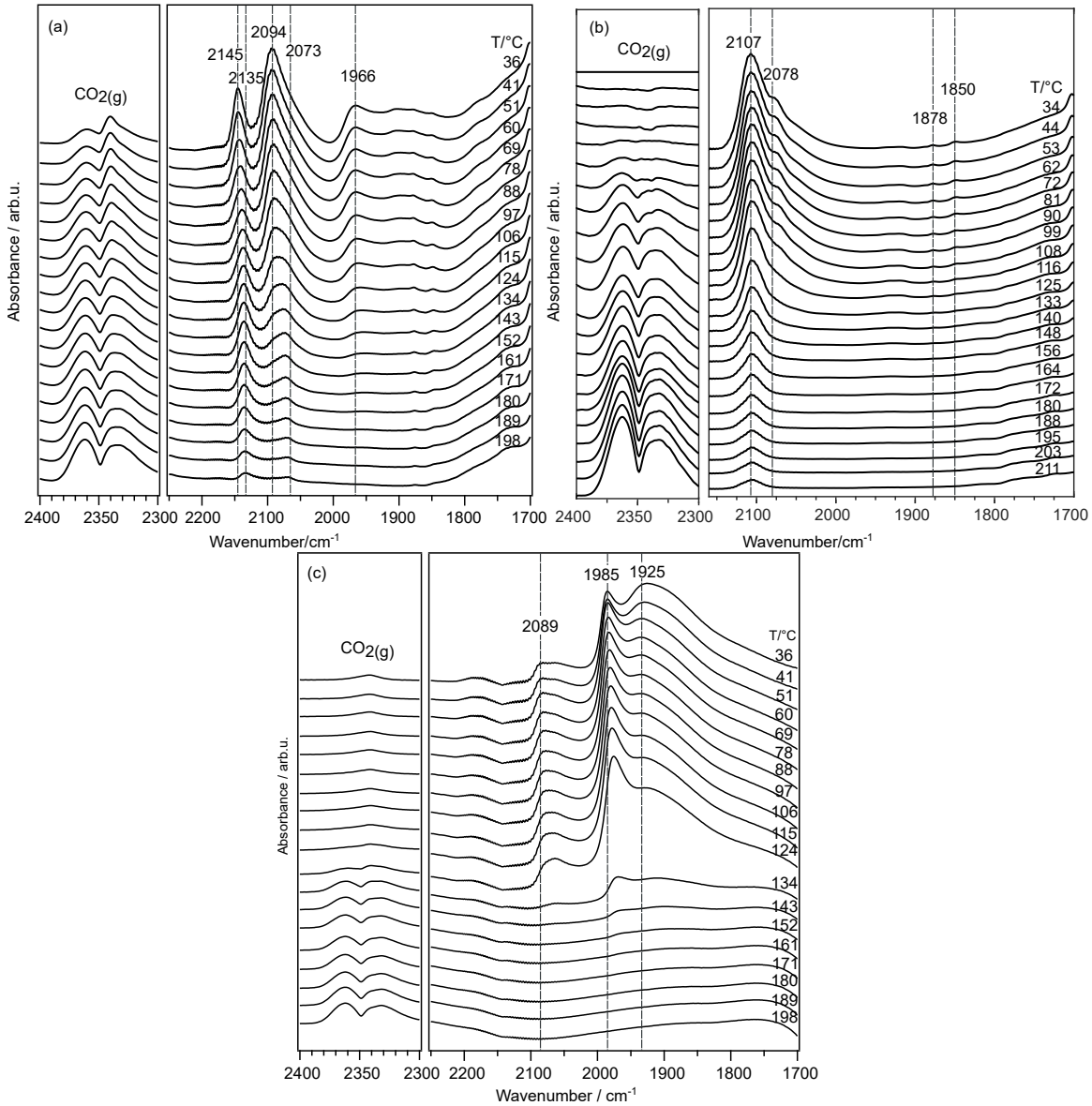

Figure 5.4: *IR spectra during CO extinction process over (a) Pd/CeO_2; (b) Pt/CeO_2, (c) 3%Pd/Al_2O_3*

Concerning the IR spectra of adsorbed CO species over 3%Pd/Al_2O_3, no CO-Pd^+ species or CO-Pd species were observed at 198 °C, meaning the adsorbed CO has fully converted into CO_2 and there were no adsorbed CO species left on the

surface. While the temperature decreased to 124 °C, a sudden build-up of both linear and bridge-bonded CO bands occurred, meanwhile, the band of gaseous CO_2 vanished. This further indicates the effect of CeO_2 support on the Pd sites.

For the alumina-supported catalysts, the CO oxidation reaction usually happens on the Pd surface, following the so-called Langmuir-Hinshelwood mechanism, where adsorbed CO species react with the dissociated O atoms on the noble metal surface, producing CO_2. In this case, under low temperatures, CO self-poisoning occurs and blocks the active sites for O_2 dissociation, leading to no CO conversion. However, CeO_2 has provided another reaction pathway (Mars-van Krevelen mechanism) that can promote the low-temperature CO oxidation ($<$ 150 °C) [132], due to the catalytic sites and the metal-ceria interface. When the temperature is lower than 150 °C, the adsorbed CO species react with the oxygen situated in the ceria support, instead of reacting with gaseous O_2 or dissociated O atoms on noble metal surface [133].

6 Conclusions and Future Work

This thesis shows that Au@Pd core@shell nanoparticles could be synthesized by a two-step seeded-growth method. The effect of temperature and Pd/Au molar ratio on the morphology of the particles was investigated. The results suggest that a thin and evenly distributed Pd shell could be obtained at 1 °C. Increasing the temperature led to a thicker and rougher shell. Moreover, increasing the Pd/Au molar ratio also makes the Pd shell thicker and rougher. Au@Pd core@shell nanoparticles with around 13 nm Au and 1.5 nm Pd shell was chosen and loaded onto γ-Al_2O_3 support by direct mixing, followed by freeze-drying. The structural and crystalline stability of the core@shell nanoparticle during the prototypical CO oxidation reaction was studied. No significant agglomeration was observed, and the core@shell structure remained intact. Blue shifts of the IR bands for adsorbed CO species were observed. The reason could be the net charge flow from Pd to Au, leading to less back-donation of electrons from Pd to CO.

To further investigate the effect of Au core on the properties of surface Pd, the systematic synthesis of Au@Pd core@shell nanoparticles catalysts with different shell/core ratios was achieved by varying the amount of precursor. The samples are denoted as Au5@Pd0.5, Au5@Pd1.5, Au13@Pd0.5, and Au13@Pd1.5. The *in situ* DRIFTS results suggest strong CO adsorption on thin-shelled catalysts, which restrict the sites for O_2 dissociation on the Pd surface. Hence, the activity towards CO oxidation over thin-shelled catalysts is relatively low. As for thick-shelled catalysts, the CO adsorption configuration is similar to Pd/Al_2O_3 catalyst.

A comparison study of CO oxidation (extinction) behaviors over highly dispersed Pd/CeO_2 and Pt/CeO_2 nanoparticle catalysts was also carried out. A similar CO configuration was observed during CO extinction process. Regardless of the complete CO conversion, adsorbed CO species on ionic Pd and Pt surfaces were observed at high temperatures, which was caused by the CeO_2 support.

The upcoming research could continue with the investigation of strain effects in $Au@Pd/Al_2O_3$ model catalyst systems. Achieving higher metal loading and scaling-up synthesis of the catalysts could be studied. Moreover, it would be interesting to perform *in situ* TEM studies during the synthesis process to further investigate the growth mechanism.

Acknowledgments

This project is financially supported by the Swedish Research Council through the project "Synergistic Development of X-ray Techniques and Applicable Thin Oxides for Sustainable Chemistry" (Dnr. 2017-06709). The study was mainly carried out at the Division of Applied Chemistry, Department of Chemistry and Chemical Engineering, Chalmers University of Technology, and partly at the Chalmers Materials Analysis Laboratory (CMAL).

I would like to thank my main supervisor Per-Anders Carlsson, co-supervisor Hanna Härelind and my examiner Martin Andersson. Thank you for helping me throughout my PhD journey. Thank you for always appreciating my work, and giving me respect, feedback, guidance, and lots of confidence in my research.

Andreas, thank you for motivating me and always helping me with the equipment and the data analysis. Jojo, thank you for your accompany and support, I appreciate all the fun times we had together. Ghodsieh, thank you for being caring and understanding. I do cherish the time we spend together. Chris, thanks for being caring, reliable, and always willing to motivate me to do more exercise. I admit you are right and I will try my best to follow your advice! Alex, thanks for being energetic and friendly. I appreciate that you are stopping me from wasting food and your company during hard times. Guido, thank you for being a super nice office mate, and a super nice brother. You always bring happiness to our office. Felix, thanks for being responsible and warm-hearted. I do appreciate your help with the technical issues. To all my group, thank you for being not only good colleagues but also good friends. Hope our friendship will not end.

I would also like to thank Stefan and Ludvig from CMAL. Thank you for assisting me with transmission electron microscopy with a lot of patience.

Many thanks to all my friends and colleagues in and outside the department. Thank you, Yin, Cansu, Qingdian, Shiyu, Jin, Mariana, Shensheng, Yiying, Ruowei, Yifei, Zhihang, and Xueting.

Last but not the least, I would like to express many thanks to my beloved family. Thank you all for your great love over the last 29 years. You always respect my decisions and support me in all aspects. You light up my life and guide me throughout the whole journey. I wish you healthy and happy, looking forward to our reunion. 最重要的是，感谢我最爱的家人。谢谢你们在过去29年对我的无私的爱。感激你们一直都尊重我的选择，并在生活上给予我无限关怀，你们照亮了我的人生。祝你们健康开心，期待我们团聚的那一天。

References

[1] Ndolomingo, M. J.; Bingwa, N.; Meijboom, R. Review of supported metal nanoparticles: synthesis methodologies, advantages and application as catalysts. *Journal of Materials Science* **2020**, *55*, 6195–6241.

[2] Fechete, I.; Wang, Y.; Védrine, J. C. The past, present and future of heterogeneous catalysis. *Catalysis Today* **2012**, *189*, 2–27.

[3] George, S. M. Introduction: heterogeneous catalysis. *Chemical Reviews* **1995**, *95*, 475–476.

[4] Belyakova, O.; Slovokhotov, Y. L. Structures of large transition metal clusters. *Russian Chemical Bulletin* **2003**, *52*, 2299–2327.

[5] Haruta, M.; Kobayashi, T.; Sano, H.; Yamada, N. Novel gold catalysts for the oxidation of carbon monoxide at a temperature far below 0 C. *Chemistry Letters* **1987**, *16*, 405–408.

[6] Malta, G.; Kondrat, S. A.; Freakley, S. J.; Davies, C. J.; Lu, L.; Dawson, S.; Thetford, A.; Gibson, E. K.; Morgan, D. J.; Jones, W., et al. Identification of single-site gold catalysis in acetylene hydrochlorination. *Science* **2017**, *355*, 1399–1403.

[7] Abad, A.; Concepción, P.; Corma, A.; García, H. A collaborative effect between gold and a support induces the selective oxidation of alcohols. *Angewandte Chemie International Edition* **2005**, *44*, 4066–4069.

[8] Pisal, D. S.; Yadav, G. D. Production of biofuel 2, 5-dimethylfuran using highly efficient single-step selective hydrogenation of 5-hydroxymethylfurfural over novel Pd-Co/Al-Zr mixed oxide catalyst. *Fuel* **2021**, *290*, 119947.

[9] Kortlever, R.; Balemans, C.; Kwon, Y.; Koper, M. T. Electrochemical CO_2 reduction to formic acid on a Pd-based formic acid oxidation catalyst. *Catalysis Today* **2015**, *244*, 58–62.

[10] Kimura, H.; Kimura, A.; Kokubo, I.; Wakisaka, T.; Mitsuda, Y. Palladium based multi-component catalytic systems for the alcohol to carboxylate oxidation reaction. *Applied Catalysis A: General* **1993**, *95*, 143–169.

[11] Choudhary, V.; Samanta, C; Choudhary, T. Direct oxidation of H_2 to H_2O_2 over Pd-based catalysts: Influence of oxidation state, support and metal additives. *Applied Catalysis A: General* **2006**, *308*, 128–133.

[12] Wang, C.; Daimon, H.; Onodera, T.; Koda, T.; Sun, S. A general approach to the size-and shape-controlled synthesis of platinum nanoparticles and their catalytic reduction of oxygen. *Angewandte Chemie* **2008**, *120*, 3644–3647.

[13] Murugavel, R.; Roesky, H. W. Titanosilicates: recent developments in synthesis and use as oxidation catalysts. *Angewandte Chemie International Edition in English* **1997**, *36*, 477–479.

[14] Ncube, P.; Hlabathe, T.; Meijboom, R. Palladium nanoparticles supported on mesoporous silica as efficient and recyclable heterogenous nanocatalysts for the Suzuki C–C coupling reaction. *Journal of Cluster Science* **2015**, *26*, 1873–1888.

[15] Hong, Z.; Wang, Z.; Li, X. Catalytic oxidation of nitric oxide (NO) over different catalysts: an overview. *Catalysis Science & Technology* **2017**, *7*, 3440–3452.

[16] Daas, B. M.; Ghosh, S Fuel cell applications of chemically synthesized zeolite modified electrode (ZME) as catalyst for alcohol electro-oxidation-a review. *Journal of Electroanalytical Chemistry* **2016**, *783*, 308–315.

[17] Tumuluri, U.; Rother, G.; Wu, Z. Fundamental understanding of the interaction of acid gases with CeO_2: from surface science to practical catalysis. *Industrial & Engineering Chemistry Research* **2016**, *55*, 3909–3919.

[18] Janssens, T. V.; Carlsson, A.; Puig-Molina, A.; Clausen, B. S. Relation between nanoscale Au particle structure and activity for CO oxidation on supported gold catalysts. *Journal of Catalysis* **2006**, *240*, 108–113.

[19] Hsu, C.; Huang, C.; Hao, Y.; Liu, F. Au/Pd core-shell nanoparticles with varied hollow Au cores for enhanced formic acid oxidation. *Nanoscale Research Letters* **2013**, *8*, 1–7.

[20] Suo, Z.; Ma, C.; Jin, M.; He, T.; An, L. The active phase of Au–Pd/Al_2O_3 for CO oxidation. *Catalysis Communications* **2008**, *9*, 2187–2190.

[21] Gong, X.; Peng, S.; Wen, W.; Sheng, P.; Li, W. Design and fabrication of magnetically functionalized core/shell microspheres for smart drug delivery. *Advanced Functional Materials* **2009**, *19*, 292–297.

[22] Fredin, L. A.; Li, Z.; Ratner, M. A.; Lanagan, M. T.; Marks, T. J. Enhanced energy storage and suppressed dielectric loss in oxide core–shell–polyolefin nanocomposites by moderating internal surface area and increasing shell thickness. *Advanced Materials* **2012**, *24*, 5946–5953.

[23] Gawande, M. B.; Goswami, A.; Asefa, T.; Guo, H.; Biradar, A. V.; Peng, D.-L.; Zboril, R.; Varma, R. S. Core–shell nanoparticles: synthesis and applications in catalysis and electrocatalysis. *Chemical Society Reviews* **2015**, *44*, 7540–7590.

[24] Schlögl, R. Heterogeneous catalysis. *Angewandte Chemie International Edition* **2015**, *54*, 3465–3520.

[25] Morbidelli, M.; Gavriilidis, A.; Varma, A., *Catalyst design*; Cambridge University Press Cambridge: 2001.

[26] Chorkendorff, I.; Niemantsverdriet, J. W., *Concepts of modern catalysis and kinetics*; John Wiley & Sons: 2017.

[27] Taylor, H. S. A theory of the catalytic surface. *Proceedings of the Royal Society of London. Series A, Containing Papers of a Mathematical and Physical Character* **1925**, *108*, 105–111.

[28] O'Neill, B. J.; Jackson, D. H.; Lee, J.; Canlas, C.; Stair, P. C.; Marshall, C. L.; Elam, J. W.; Kuech, T. F.; Dumesic, J. A.; Huber, G. W. Catalyst design with atomic layer deposition. *Acs Catalysis* **2015**, *5*, 1804–1825.

[29] Ghosh Chaudhuri, R.; Paria, S. Core/shell nanoparticles: classes, properties, synthesis mechanisms, characterization, and applications. *Chemical Reviews* **2012**, *112*, 2373–2433.

[30] Ahmed, J.; Ahmad, T.; Ramanujachary, K. V.; Lofland, S. E.; Ganguli, A. K. Development of a microemulsion-based process for synthesis of cobalt (Co) and cobalt oxide (Co_3O_4) nanoparticles from submicrometer rods of cobalt oxalate. *Journal of Colloid and Interface Science* **2008**, *321*, 434–441.

[31] Lu, C.-L.; Prasad, K. S.; Wu, H.-L.; Ho, J.-a. A.; Huang, M. H. Au nanocube-directed fabrication of Au-Pd core-shell nanocrystals with tetrahexahedral, concave octahedral, and octahedral structures and their electrocatalytic activity. *Journal of the American Chemical Society* **2010**, *132*, 14546–14553.

[32] Tajarenejad, H.; Ansari, M. A.; Akbari, S.; Yazdanfar, H.; Hamidi, S. M. Optical neural stimulation using the thermoplasmonic effect of gold nano-hexagon. *Biomedical Optics Express* **2021**, *12*, 6013–6023.

[33] Sankar, M.; He, Q.; Engel, R. V.; Sainna, M. A.; Logsdail, A. J.; Roldan, A.; Willock, D. J.; Agarwal, N.; Kiely, C. J.; Hutchings, G. J. Role of the support in gold-containing nanoparticles as heterogeneous catalysts. *Chemical Reviews* **2020**, *120*, 3890–3938.

[34] Satsuma, A.; Osaki, K.; Yanagihara, M.; Ohyama, J.; Shimizu, K. Activity controlling factors for low-temperature oxidation of CO over supported Pd catalysts. *Applied Catalysis B: Environmental* **2013**, *132*, 511–518.

[35] Petrov, A. W.; Ferri, D.; Krumeich, F.; Nachtegaal, M.; van Bokhoven, J. A.; Kröcher, O. Stable complete methane oxidation over palladium based zeolite catalysts. *Nature Communications* **2018**, *9*, 1–8.

[36] Carlsson, P.-A.; Fridell, E.; Skoglundh, M. Methane oxidation over Pt/Al_2O_3 and Pd/Al_2O_3 catalysts under transient conditions. *Catalysis Letters* **2007**, *115*, 1–7.

[37] Mayernick, A. D.; Janik, M. J. Methane oxidation on Pd–Ceria: A DFT study of the mechanism over $PdxCe_1 - xO_2$, Pd, and PdO. *Journal of Catalysis* **2011**, *278*, 16–25.

[38] Nilsson, J.; Carlsson, P.-A.; Fouladvand, S.; Martin, N. M.; Gustafson, J.; Newton, M. A.; Lundgren, E.; Gronbeck, H.; Skoglundh, M. Chemistry of supported palladium nanoparticles during methane oxidation. *ACS Catalysis* **2015**, *5*, 2481–2489.

[39] Nilsson, J.; Carlsson, P.-A.; Martin, N. M.; Adams, E. C.; Agostini, G.; Grönbeck, H.; Skoglundh, M. Methane oxidation over Pd/Al_2O_3 under rich/lean cycling followed by operando XAFS and modulation excitation spectroscopy. *Journal of Catalysis* **2017**, *356*, 237–245.

[40] Nilsson, J.; Carlsson, P.-A.; Martin, N. M.; Velin, P.; Meira, D. M.; Grönbeck, H.; Skoglundh, M. Oxygen step-response experiments for methane oxidation over Pd/Al_2O_3: An in situ XAFS study. *Catalysis Communications* **2018**, *109*, 24–27.

[41] Velin, P.; Ek, M.; Skoglundh, M.; Schaefer, A.; Raj, A.; Thompsett, D.; Smedler, G.; Carlsson, P.-A. Water inhibition in methane oxidation over alumina supported palladium catalysts. *The Journal of Physical Chemistry C* **2019**, *123*, 25724–25737.

[42] Velin, P.; Florén, C.-R.; Skoglundh, M.; Raj, A.; Thompsett, D.; Smedler, G.; Carlsson, P.-A. Palladium dispersion effects on wet methane oxidation kinetics. *Catalysis Science & Technology* **2020**, *10*, 5460–5469.

[43] Velin, P.; Hemmingsson, F.; Schaefer, A.; Skoglundh, M.; Lomachenko, K. A.; Raj, A.; Thompsett, D.; Smedler, G.; Carlsson, P.-A. Hampered PdO redox dynamics by water suppresses lean methane oxidation over realistic palladium catalysts. *ChemCatChem* **2021**, *13*, 3765–3771.

[44] Kim, K. B.; Kim, M. K.; Kim, Y. H.; Song, K. S.; Park, E. D. Propane combustion over supported Pd catalysts. *Research on Chemical Intermediates* **2010**, *36*, 603–611.

[45] Carlsson, P.-A.; Mollner, S.; Arnby, K.; Skoglundh, M. Effect of periodic operation on the low-temperature activity for propane oxidation over Pt/Al_2O_3 catalysts. *Chemical Engineering Science* **2004**, *59*, 4313–4323.

[46] Carlsson, P.-A.; Skoglundh, M.; Fridell, E.; Jobson, E.; Andersson, B. Induced low temperature catalytic ignition by transient changes in the gas composition. *Catalysis Today* **2002**, *73*, 307–313.

[47] Carlsson, P.-A.; Skoglundh, M.; Thormählen, P.; Andersson, B. Low-temperature CO oxidation over a Pt/Al_2O_3 monolith catalyst investigated by step-response experiments and simulations. *Topics in Catalysis* **2004**, *30*, 375–381.

[48] Carlsson, P.-A.; Zhdanov, V. P.; Skoglundh, M. Self-sustained kinetic oscillations in CO oxidation over silica-supported Pt. *Physical Chemistry Chemical Physics* **2006**, *8*, 2703–2706.

[49] Visser, T.; Nijhuis, T. A.; Van Der Eerden, A. M.; Jenken, K.; Ji, Y.; Bras, W.; Nikitenko, S.; Ikeda, Y.; Lepage, M.; Weckhuysen, B. M. Promotion effects in the oxidation of CO over zeolite-supported Pt nanoparticles. *The Journal of Physical Chemistry B* **2005**, *109*, 3822–3831.

[50] Bond, G. C.; Louis, C.; Thompson, D., *Catalysis by gold*; World Scientific: 2006; Vol. 6.

[51] Becker, E.; Carlsson, P.-A.; Kylhammar, L.; Newton, M. A.; Skoglundh, M. In situ spectroscopic investigation of low-temperature oxidation of methane over alumina-supported platinum during periodic operation. *The Journal of Physical Chemistry C* **2011**, *115*, 944–951.

[52] Tauster, S.; Fung, S.; Garten, R. L. Strong metal-support interactions. Group 8 noble metals supported on titanium dioxide. *Journal of the American Chemical Society* **1978**, *100*, 170–175.

[53] Widmann, D.; Liu, Y.; Schüth, F.; Behm, R. J. Support effects in the Au-catalyzed CO oxidation–Correlation between activity, oxygen storage capacity, and support reducibility. *Journal of Catalysis* **2010**, *276*, 292–305.

[54] Eguchi, K.; Arai, H. Low temperature oxidation of methane over Pd-based catalysts—effect of support oxide on the combustion activity. *Applied Catalysis A: General* **2001**, *222*, 359–367.

[55] Kim, D. H.; Lim, M. S. Kinetics of selective CO oxidation in hydrogen-rich mixtures on Pt/alumina catalysts. *Applied Catalysis A: General* **2002**, *224*, 27–38.

[56] Lou, Y.; Xu, J.; Zhang, Y.; Pan, C.; Dong, Y.; Zhu, Y. Metal-support interaction for heterogeneous catalysis: from nanoparticles to single atoms. *Materials Today Nano* **2020**, 100093.

[57] Duan, S.; Senkan, S. Catalytic conversion of ethanol to hydrogen using combinatorial methods. *Industrial & Engineering Chemistry Research* **2005**, *44*, 6381–6386.

[58] He, Z.; Yang, M.; Wang, X.; Zhao, Z.; Duan, A. Effect of the transition metal oxide supports on hydrogen production from bio-ethanol reforming. *Catalysis Today* **2012**, *194*, 2–8.

[59] Hayek, K; Kramer, R; Paál, Z Metal-support boundary sites in catalysis. *Applied Catalysis A: General* **1997**, *162*, 1–15.

[60] Schlexer, P.; Ruiz Puigdollers, A.; Pacchioni, G. Role of metal/oxide interfaces in enhancing the local oxide reducibility. *Topics in Catalysis* **2019**, *62*, 1192–1201.

[61] Liu, L.; Corma, A. Metal catalysts for heterogeneous catalysis: from single atoms to nanoclusters and nanoparticles. *Chemical Reviews* **2018**, *118*, 4981–5079.

[62] Smith, A. M.; Mohs, A. M.; Nie, S. Tuning the optical and electronic properties of colloidal nanocrystals by lattice strain. *Nature Nanotechnology* **2009**, *4*, 56–63.

[63] Wang, S.; Omidvar, N.; Marx, E.; Xin, H. Coordination numbers for unraveling intrinsic size effects in gold-catalyzed CO oxidation. *Physical Chemistry Chemical Physics* **2018**, *20*, 6055–6059.

[64] Sinfelt, J. H.; Meitzner, G. D. X-ray absorption edge studies of the electronic structure of metal catalysts. *Accounts of Chemical Research* **1993**, *26*, 1–6.

[65] Kitchin, J.; Nørskov, J. K.; Barteau, M.; Chen, J. Modification of the surface electronic and chemical properties of Pt (111) by subsurface 3d transition metals. *The Journal of Chemical Physics* **2004**, *120*, 10240–10246.

[66] Xia, Z.; Guo, S. Strain engineering of metal-based nanomaterials for energy electrocatalysis. *Chemical Society Reviews* **2019**, *48*, 3265–3278.

[67] Kuo, C.-H.; Lamontagne, L. K.; Brodsky, C. N.; Chou, L.-Y.; Zhuang, J.; Sneed, B. T.; Sheehan, M. K.; Tsung, C.-K. The effect of lattice strain on the catalytic properties of Pd nanocrystals. *ChemSusChem* **2013**, *6*, 1993–2000.

[68] Strasser, P.; Koh, S.; Anniyev, T.; Greeley, J.; More, K.; Yu, C.; Liu, Z.; Kaya, S.; Nordlund, D.; Ogasawara, H., et al. Lattice-strain control of the activity in dealloyed core–shell fuel cell catalysts. *Nature Chemistry* **2010**, *2*, 454–460.

[69] Nilsson, A; Pettersson, L.; Hammer, B; Bligaard, T; Christensen, C.; Nørskov, J. The electronic structure effect in heterogeneous catalysis. *Catalysis Letters* **2005**, *100*, 111–114.

[70] Hammer, B.; Nørskov, J. K. Theoretical surface science and catalysis—calculations and concepts. *Advances in Catalysis* **2000**, *45*, 71–129.

[71] Yi, C.-W.; Luo, K; Wei, T; Goodman, D. The composition and structure of Pd- Au surfaces. *The Journal of Physical Chemistry B* **2005**, *109*, 18535–18540.

[72] Kitchin, J. R.; Nørskov, J. K.; Barteau, M. A.; Chen, J. Role of strain and ligand effects in the modification of the electronic and chemical properties of bimetallic surfaces. *Physical Review Letters* **2004**, *93*, 156801.

[73] Laskar, M; Skrabalak, S. A balancing act: manipulating reactivity of shape-controlled metal nanocatalysts through bimetallic architecture. *Journal of Materials Chemistry A* **2016**, *4*, 6911–6918.

[74] Ponec, V.; Bond, G. C., *Catalysis by metals and alloys*; Elsevier: 1995; Vol. 95.

[75] Zafeiratos, S.; Piccinin, S.; Teschner, D. Alloys in catalysis: phase separation and surface segregation phenomena in response to the reactive environment. *Catalysis Science & Technology* **2012**, *2*, 1787–1801.

[76] Chen, J.; Finfrock, Y. Z.; Wang, Z.; Sham, T.-K. Strain and ligand effects in Pt-Ni alloys studied by valence-to-core X-ray emission spectroscopy. *Scientific Reports* **2021**, *11*, 1–8.

[77] Martin, N. M.; Skoglundh, M.; Smedler, G.; Raj, A.; Thompsett, D.; Velin, P.; Martinez-Casado, F. J.; Matej, Z.; Balmes, O.; Carlsson, P.-A. CO oxidation and site speciation for alloyed palladium–platinum model catalysts studied by in situ FTIR spectroscopy. *The Journal of Physical Chemistry C* **2017**, *121*, 26321–26329.

[78] Martin, N. M.; Nilsson, J.; Skoglundh, M.; Adams, E. C.; Wang, X.; Velin, P.; Smedler, G.; Raj, A.; Thompsett, D.; Brongersma, H. H., et al. Characterization of surface structure and oxidation/reduction behavior of Pd–Pt/Al_2O_3 model catalysts. *The Journal of Physical Chemistry C* **2016**, *120*, 28009–28020.

[79] Martin, N. M.; Nilsson, J.; Skoglundh, M.; Adams, E. C.; Wang, X.; Smedler, G.; Raj, A.; Thompsett, D.; Agostini, G.; Carlson, S., et al. Study of methane oxidation over alumina supported Pd–Pt catalysts using operando DRIFTS/MS and in situ XAS techniques. *Catalysis, Structure & Reactivity* **2017**, *3*, 24–32.

[80] Xu, J.; White, T.; Li, P.; He, C.; Yu, J.; Yuan, W.; Han, Y.-F. Biphasic Pd-Au alloy catalyst for low-temperature CO oxidation. *Journal of the American Chemical Society* **2010**, *132*, 10398–10406.

[81] Hu, W.; Wu, Y.; Chen, J.; Qu, P.; Zhong, L.; Chen, Y. Methane combustion with a Pd–Pt catalyst stabilized by magnesia–alumina spinel in a high-humidity feed. *Industrial & Engineering Chemistry Research* **2020**, *59*, 11170–11176.

[82] Liu, G.; Walsh, A. G.; Zhang, P. Synergism of iron and platinum species for low-temperature CO oxidation: from two-dimensional surface to nanoparticle and single-atom catalysts. *The Journal of Physical Chemistry Letters* **2020**, *11*, 2219–2229.

[83] Koutsopoulos, S.; Eriksen, K. M.; Fehrmann, R. Synthesis and characterization of supported Pt and Pt alloys nanoparticles used for the catalytic oxidation of sulfur dioxide. *Journal of Catalysis* **2006**, *238*, 270–276.

[84] Borah, R.; Verbruggen, S. W. Silver–gold bimetallic alloy versus core–shell nanoparticles: Implications for plasmonic enhancement and photothermal applications. *The Journal of Physical Chemistry C* **2020**, *124*, 12081–12094.

[85] Zeng, J.; Yang, J.; Lee, J. Y.; Zhou, W. Preparation of carbon-supported core-shell Au-Pt nanoparticles for methanol oxidation reaction: The promotional effect of the Au Core. *The Journal of Physical Chemistry B* **2006**, *110*, 24606–24611.

[86] Yin, H.; Ma, Z.; Chi, M.; Dai, S. Heterostructured catalysts prepared by dispersing Au@Fe_2O_3 core–shell structures on supports and their performance in CO oxidation. *Catalysis Today* **2011**, *160*, 87–95.

[87] Li, L.; Zhang, N.; Wu, R.; Song, L.; Zhang, G.; He, H. Comparative study of moisture-treated Pd@CeO_2/Al_2O_3 and Pd/CeO_2/Al_2O_3 catalysts for automobile exhaust emission reactions: effect of core–shell interface. *ACS Applied Materials & Interfaces* **2020**, *12*, 10350–10358.

[88] Hosseini, M; Barakat, T; Cousin, R; Aboukaïs, A; Su, B.-L.; De Weireld, G; Siffert, S Catalytic performance of core–shell and alloy Pd–Au nanoparticles for total oxidation of VOC: The effect of metal deposition. *Applied Catalysis B: Environmental* **2012**, *111*, 218–224.

[89] Edwards, J. K.; Solsona, B. E.; Landon, P.; Carley, A. F.; Herzing, A.; Kiely, C. J.; Hutchings, G. J. Direct synthesis of hydrogen peroxide from H_2 and O_2 using TiO_2-supported Au–Pd catalysts. *Journal of Catalysis* **2005**, *236*, 69–79.

[90] Sietsma, J. R.; Van Dillen, A. J.; De Jongh, P. E.; De Jong, K. P. In *Studies in Surface Science and Catalysis*; Elsevier: 2006; Vol. 162, pp 95–102.

[91] Haukka, S.; Lakomaa, E.-L.; Suntola, T. In *Studies in Surface Science and Catalysis*; Elsevier: 1999; Vol. 120, pp 715–750.

[92] Munnik, P.; de Jongh, P. E.; de Jong, K. P. Recent developments in the synthesis of supported catalysts. *Chemical Reviews* **2015**, *115*, 6687–6718.

[93] Van Honschoten, J. W.; Brunets, N.; Tas, N. R. Capillarity at the nanoscale. *Chemical Society Reviews* **2010**, *39*, 1096–1114.

[94] Niu, W.; Zhang, L.; Xu, G. Seed-mediated growth of noble metal nanocrystals: crystal growth and shape control. *Nanoscale* **2013**, *5*, 3172–3181.

[95] Murphy, C. J.; Sau, T. K.; Gole, A. M.; Orendorff, C. J.; Gao, J.; Gou, L.; Hunyadi, S. E.; Li, T. Anisotropic metal nanoparticles: synthesis, assembly, and optical applications. *The Journal of Physical Chemistry B* **2005**, *109*, 13857–13870.

[96] Zhang, Q.; Xie, J.; Yu, Y.; Yang, J.; Lee, J. Y. Tuning the crystallinity of Au nanoparticles. *Small* **2010**, *6*, 523–527.

[97] Liu, M.; Guyot-Sionnest, P. Mechanism of silver (I)-assisted growth of gold nanorods and bipyramids. *The Journal of Physical Chemistry B* **2005**, *109*, 22192–22200.

[98] Jana, N. R. Gram-scale synthesis of soluble, near-monodisperse gold nanorods and other anisotropic nanoparticles. *Small* **2005**, *1*, 875–882.

[99] Feng, C.; Liu, X.; Zhu, T.; Tian, M. Catalytic oxidation of CO on noble metal-based catalysts. *Environmental Science and Pollution Research* **2021**, 1–25.

[100] Wu, H.-L.; Kuo, C.-H.; Huang, M. H. Seed-mediated synthesis of gold nanocrystals with systematic shape evolution from cubic to trisoctahedral and rhombic dodecahedral structures. *Langmuir* **2010**, *26*, 12307–12313.

[101] Zhang, C.; Gustafson, J.; Merte, L. R.; Evertsson, J.; Norén, K.; Carlson, S.; Svensson, H.; Carlsson, P.-A. An in situ sample environment reaction cell for spatially resolved X-ray absorption spectroscopy studies of powders and small structured reactors. *Review of Scientific Instruments* **2015**, *86*, 033112.

[102] Winey, M.; Meehl, J. B.; O'Toole, E. T.; Giddings Jr, T. H. Conventional transmission electron microscopy. *Molecular Biology of the Cell* **2014**, *25*, 319–323.

[103] Wang, Z. Transmission electron microscopy of shape-controlled nanocrystals and their assemblies. *The Journal of Physical Chemistry B* **2000**, *104*, 1153–1175.

[104] Williams, D. B.; Carter, C. B. Transmission electron microscopy plenum press. *New York and London* **1996**.

[105] Wang, J.; Chen, H.; Hu, Z.; Yao, M.; Li, Y. A review on the Pd-based three-way catalyst. *Catalysis Reviews* **2015**, *57*, 79–144.

[106] Stanjek, H; Häusler, W. Basics of X-ray diffraction. *Hyperfine Interactions* **2004**, *154*, 107–119.

[107] Hollander, J. M.; Jolly, W. L. X-ray photoelectron spectroscopy. *Accounts of chemical research* **1970**, *3*, 193–200.

[108] Van der Heide, P., *X-ray photoelectron spectroscopy: an introduction to principles and practices*; John Wiley & Sons: 2011.

[109] Rotole, J. A.; Sherwood, P. M. Gamma-alumina (γ-Al2O3) by XPS. *Surface Science Spectra* **1998**, *5*, 18–24.

[110] Theis, W.; Horn, K. Temperature-dependent line broadening in core-level photoemission spectra from aluminum. *Physical Review B* **1993**, *47*, 16060–16063.

[111] Campbell, J.; Papp, T. Widths of the atomic K–N7 levels. *Atomic Data and Nuclear Data Tables* **2001**, *77*, 1–56.

[112] Thomsen, V. Basic fundamental parameters in x-ray fluorescence. *Spectroscopy-Springfield then Eugene then Duluth-* **2007**, *22*, 46.

[113] Potts, P. J.; Webb, P. C. X-ray fluorescence spectrometry. *Journal of Geochemical Exploration* **1992**, *44*, 251–296.

[114] Ng, L. M.; Simmons, R. Infrared spectroscopy. *Analytical Chemistry* **1999**, *71*, 343–350.

[115] Stuart, B. H., *Infrared spectroscopy: fundamentals and applications*; John Wiley & Sons: 2004.

[116] Stuart, B. Infrared spectroscopy. *Kirk-Othmer Encyclopedia of Chemical Technology* **2000**.

[117] Hanrahan, P.; Krueger, W. In *Proceedings of the 20th annual conference on Computer graphics and interactive techniques*, 1993, pp 165–174.

[118] Günzler, H.; Gremlich, H.-U. IR spectroscopy. An introduction. **2002**.

[119] Piella, J.; Bastus, N. G.; Puntes, V. Size-controlled synthesis of sub-10-nanometer citrate-stabilized gold nanoparticles and related optical properties. *Chemistry of Materials* **2016**, *28*, 1066–1075.

[120] Hu, J.-W.; Zhang, Y.; Li, J.-F.; Liu, Z.; Ren, B.; Sun, S.-G.; Tian, Z.-Q.; Lian, T. Synthesis of Au@ Pd core–shell nanoparticles with controllable size and their application in surface-enhanced Raman spectroscopy. *Chemical Physics Letters* **2005**, *408*, 354–359.

[121] Xia, Y.; Xia, X.; Peng, H.-C. Shape-controlled synthesis of colloidal metal nanocrystals: thermodynamic versus kinetic products. *Journal of the American Chemical Society* **2015**, *137*, 7947–7966.

[122] Li, J.; Zheng, Y.; Zeng, J.; Xia, Y. Controlling the size and morphology of Au@Pd core–shell nanocrystals by manipulating the kinetics of seeded growth. *Chemistry–A European Journal* **2012**, *18*, 8150–8156.

[123] Tan, S. F.; Chee, S. W.; Lin, G.; Bosman, M.; Lin, M.; Mirsaidov, U.; Nijhuis, C. A. Real-time imaging of the formation of Au–Ag core–shell nanoparticles. *Journal of the American Chemical Society* **2016**, *138*, 5190–5193.

[124] Tan, S. F.; Bisht, G.; Anand, U.; Bosman, M.; Yong, X. E.; Mirsaidov, U. In situ kinetic and thermodynamic growth control of Au–Pd core–shell nanoparticles. *Journal of the American Chemical Society* **2018**, *140*, 11680–11685.

[125] Sárkány, A.; Geszti, O.; Sáfrán, G. Preparation of Pdshell–Aucore/SiO_2 catalyst and catalytic activity for acetylene hydrogenation. *Applied Catalysis A: General* **2008**, *350*, 157–163.

[126] Kariuki, V. M.; Hoffmeier, J. C.; Yazgan, I.; Sadik, O. A. Seedless synthesis and SERS characterization of multi-branched gold nanoflowers using water soluble polymers. *Nanoscale* **2017**, *9*, 8330–8340.

[127] Xie, J.; Zhang, Q.; Lee, J. Y.; Wang, D. I. The synthesis of SERS-active gold nanoflower tags for in vivo applications. *ACS Nano* **2008**, *2*, 2473–2480.

[128] Zhang, P.; Xiahou, Y.; Wang, J.; Hang, L.; Wang, D.; Xia, H. Revitalizing spherical Au@Pd nanoparticles with controlled surface-defect density as high performance electrocatalysts. *Journal of Materials Chemistry A* **2017**, *5*, 6992–7000.

[129] Zhu, H.; Gao, G.; Du, M.; Zhou, J.; Wang, K.; Wu, W.; Chen, X.; Li, Y.; Ma, P.; Dong, W., et al. Atomic-scale core/shell structure engineering induces precise tensile strain to boost hydrogen evolution catalysis. *Advanced Materials* **2018**, *30*, 1707301.

[130] Compounds, O. Calculations of Electron Inelastic Mean Free Paths. **1993**, *21*, 165–176.

[131] Zhou, G.-F.; Ma, J.; Bai, S.; Wang, L.; Guo, Y. CO catalytic oxidation over Pd/CeO_2 with different chemical states of Pd. *Rare Metals* **2020**, *39*, 800–805.

[132] Cargnello, M.; Doan-Nguyen, V. V.; Gordon, T. R.; Diaz, R. E.; Stach, E. A.; Gorte, R. J.; Fornasiero, P.; Murray, C. B. Control of metal nanocrystal size reveals metal-support interface role for ceria catalysts. *Science* **2013**, *341*, 771–773.

[133] Li, H.; Shen, M.; Wang, J.; Wang, H.; Wang, J. Effect of support on CO oxidation performance over the Pd/CeO_2 and Pd/CeO_2–ZrO_2 catalyst. *Industrial & Engineering Chemistry Research* **2020**, *59*, 1477–1486.